



Contents lists available at ScienceDirect

Geochimica et Cosmochimica Acta

journal homepage: www.elsevier.com/locate/gca

Trace element partitioning in silica-undersaturated alkaline magmatic systems



Sander M. Molendijk^{a,*}, Olivier Namur^a, Paul R.D. Mason^b, Benoît Dubacq^c, Benoît Smets^{d,e}, David A. Neave^f, Bernard Charlier^g

^a Department of Earth and Environmental Sciences, KU Leuven, Celestijnenlaan 200E, 3001 Leuven, Belgium

^b Department of Earth Sciences, Utrecht University, Princetonlaan 8A, 3584 CB Utrecht, the Netherlands

^c Sorbonne Université, CNRS-INSU, Institut des Sciences de la Terre Paris, IStEP, UMR 7193, F-75005 Paris, France

^d Department of Earth Sciences, Royal Museum for Central Africa, Leuvensesteenweg 13, B-3080 Tervuren, Belgium

^e Department of Geography, Vrije Universiteit Brussel, Pleinlaan 2, B-1050 Brussels, Belgium

^f Department of Earth and Environmental Sciences, The University of Manchester, Oxford Road, Manchester M13 9PL, United Kingdom

^g Département de Géologie, Université de Liège, B-4000 Liège, Belgium

ARTICLE INFO

Article history:

Received 11 August 2022

Accepted 25 January 2023

Available online 2 February 2023

Associate editor: James Van Orman

Keywords:

Alkaline magmatism

Partition coefficients

Feldspathoids

Nyiragongo

Experimental petrology

ABSTRACT

Alkaline magmatism is an important chemical end-member of magmatic activity that typically occurs in response to small volume melting of asthenospheric- and/or lithospheric mantle material in intra-continental settings. Understanding trace element partitioning and phase equilibria during alkaline magmatism can therefore provide constraints on intra-continental geodynamic settings. However, the partitioning of trace elements between alkaline melts and their dominant equilibrium mineral phases remains poorly constrained. Feldspathoids in particular have received limited attention with regards to their trace element contents, hampering our ability to interpret geochemical trends in alkaline magmatic systems. In this study, we performed a series of 1 atmosphere experiments in a gas-mixing furnace using a variety of highly alkaline ($\text{Na}_2\text{O} + \text{K}_2\text{O} = 4.15\text{--}14.97 \text{ wt}\%$) and silica-undersaturated ($\text{SiO}_2 = 36.73\text{--}45.96 \text{ wt}\%$) lava compositions from Nyiragongo, Democratic Republic of Congo, in order to investigate the partitioning behaviour of trace elements in minerals from alkaline magmas. Experimental runs were performed with oxygen fugacity buffered at both QFM (quartz-fayalite-magnetite equilibrium) and QFM + 1 and cover a range of geologically-relevant temperatures (1025–1200 °C). The quenched products of these experiments contained leucite, nepheline, melilite, clinopyroxene, olivine, and rhönite crystals, of which glass-crystal pairs were analysed for rare earth elements, large-ion lithophile elements, and high-field-strength elements. Leucite and nepheline host considerable quantities of large-ion lithophile elements but take up negligible amounts of more highly charged cations. Åkermanitic melilite readily incorporates mono- to trivalent cations with a preference for light over heavy rare earth elements, but incorporates only select divalent cations. Rhönite and clinopyroxene have analogous partitioning behaviours, with a strong preference for heavy over light rare earth elements. Fractionation modelling using the reported partitioning behaviours reproduces the 2021 eruption products of Nyiragongo, with 48% fractionation from an olivine-melilitic parental melt composition. Crystallization of trace-element poor feldspathoid amplifies pre-existing high LREE/MREE ratios of the parental magma and progressively increase trace element abundances for all but monovalent cations.

© 2023 Elsevier Ltd. All rights reserved.

1. Introduction

Modelling of elemental distributions in mineral assemblages is essential to the decryption of whole-rock compositional trends and magmatic processes as a whole (e.g., Sun and Hanson, 1976;

Mittlefehldt and Miller, 1983; Keppler, 1996; Taura et al., 1998; Matzen et al., 2017; Namur and Humphreys, 2018). However, such modelling requires detailed knowledge of partition coefficients, which is not always readily available, especially for silica-undersaturated systems. Here we investigate mineral-melt partitioning for the lavas of the highly alkali-rich, silica-undersaturated Nyiragongo volcano in the Democratic Republic (DR) of Congo. Samples from this magmatic system have been

* Corresponding author.

E-mail address: sander.molendijk@kuleuven.be (S.M. Molendijk).

reported as unusually enriched in large-ion lithophile elements (LILE) and light rare earth elements (LREE), although the reason for this remains uncertain (Hertogen et al., 1985; Platz et al., 2004; Chakrabarti et al., 2009). Quantifying the behaviour of trace elements during melting and fractional crystallization is essential for explaining the origin of these enrichments, in particular for discerning between primary enrichment inherited from the source (Platz et al., 2004; Chakrabarti et al., 2009) and secondary enrichment driven by fractionation (e.g., Hertogen et al., 1985).

The partitioning behaviour of trace elements between melt and minerals has been studied for decades (e.g., Jensen 1973; Hart and Dunn 1993; Blundy and Wood 2003; Dubacq and Plunder 2018), either through the use of glass/groundmass-mineral pairs in rapidly quenched rocks (Onuma et al., 1968, 1981; Fujimaki, 1986; Minissale et al., 2019), (Hart and Dunn, 1993; Dygert et al., 2014), or theoretical methods (Blundy and Wood, 1994; Van Westrenen et al., 2000; Dubacq and Plunder, 2018). Extensive literature is therefore available on partitioning behaviour for minerals commonly crystallizing from tholeiitic magmas such as clinopyroxene (e.g., Skulski et al., 1994; Johnson, 1998; Green et al., 2000; Hill et al., 2011; Bédard, 2014; Dygert et al., 2014; Shepherd et al., 2022), olivine (e.g., Irving, 1978; Beattie et al., 1991; Beattie, 1993; Taura et al., 1998; Bédard, 2005; Evans et al., 2008) and plagioclase (e.g., Bédard, 2006; Aigner-Torres et al., 2007; Tepley et al., 2010; Sun et al., 2017; Dygert et al., 2020), but data remain limited for minerals solely formed from silica-undersaturated magmas (e.g., leucite, melilite, nepheline). Published partition coefficients between feldspathoids and melt are based mainly on phenocryst-matrix observations (Onuma et al., 1981; Ewart and Griffin, 1994; Foley and Jenner, 2004; Arzamastsev et al., 2009; Minissale et al., 2019). While such studies provide first-order insights, they are frequently influenced by crystal-melt disequilibrium, crystal zoning, incomplete quenching of the matrix and contamination of analyses by mineral or melt inclusions leading to anomalous results (Albarede and Bottinga, 1972; Lee et al., 2007). Furthermore, the few experimental studies performed with compositions crystallizing such minerals sometimes omitted alkali metals entirely in their starting compositions (Nagasawa et al., 1980; Lundstrom et al., 2006; Ustunisik et al., 2019), filtering out any potential effect of these elements on the partitioning behaviour. The frequently reported influence of crystal and melt compositions on trace element partitioning (Beckett et al., 1990; Dubacq and Plunder, 2018; Beard et al., 2019) render coefficients derived from such studies potentially unreliable for application to alkali-rich natural lavas. This hampers geochemical interpretation in active alkali-rich, silica-undersaturated magmatic regions including the circum-Mediterranean region (Lustrino and Wilson, 2007), the West Antarctic rift system (Kyle et al., 1992; Martin et al., 2013), and the East African rift system (Platz et al., 2004; Klaudius and Keller, 2006).

In this study, partition coefficients for a variety of minerals common to (per)alkaline magmatic systems were determined under dry conditions at a pressure of 1 bar. Studied minerals include leucite (KAlSi_2O_6), melilite ($(\text{Ca},\text{Na})_2(\text{Al},\text{Mg},\text{Fe})(\text{Si},\text{Al})\text{O}_7$), clinopyroxene, olivine, nepheline ($\text{KNa}_3\text{Al}_4\text{Si}_4\text{O}_{16}$) and rhönite ($(\text{Ca},\text{Na})_2(\text{Mg},\text{Fe}^{2+/3+}, \text{Ti})_6(\text{Si},\text{Al},\text{Fe}^{3+})_6\text{O}_{20}$). The relevance of these partition coefficients was tested for the Nyiragongo volcanic system, allowing for forward modelling of the trace element evolution of alkaline lavas more generally during fractional crystallization.

2. Nyiragongo volcano

Nyiragongo is an active volcano in the DR Congo, and one of the eight major volcanoes of the Virunga Volcanic Province (VVP) located in the western branch of the East African Rift system,

generally characterized by the presence of a persistent lava lake in its summit crater (Tazieff, 1949, 1984; Durieux, 2002; Barrière et al., 2022). Nyiragongo is among the most active volcanoes on Earth (Wright et al., 2015) and threatens the city of Goma, which was impacted by flank eruptions in 1977, 2002, and 2021, which drained the lava lake system at that time (e.g., Pottier, 1978; Komorowski et al., 2002; Barrière et al., 2022). The lava field of Nyiragongo is also characterised by numerous parasitic cones mostly located at the foot of the main edifice or along radial fracture zones, some of which erupted explosively (Poppe et al., 2016). The Nyiragongo volcano is known for the unusual, highly alkaline ($\text{Na}_2\text{O} + \text{K}_2\text{O} = 6.3\text{--}13.7$ wt%; Platz et al. 2004) composition of its main crater lavas (e.g., Sahama 1962; Demant et al. 1994; Platz et al. 2004). The high alkalinity of Nyiragongo's volcanic products is associated with silica-undersaturation ($\text{SiO}_2 = 35.7\text{--}39.0$ wt%; Barette et al. 2017; Fig. 1), generating some of the lowest viscosity lavas on Earth (Giordano et al., 2007; Morrison et al., 2020). Magmatism in the VVP started in the Late Miocene and was related to the doming stage of the development of the Kivu rift (Poucllet et al., 2016). A compositional transition of the erupted material from sodic alkaline- to potassic alkaline lavas occurred in the late Pliocene (Poucllet et al., 2016). The exact nature of the potassic source is still debated, with primary hypotheses focusing on metasomatic sources of either lithospheric or deep mantle origins (Chakrabarti et al., 2009; Furman et al., 2015). Nyiragongo itself experienced a transition from more explosive, melilite dominated magmatism to more nepheline-dominated lavas (Sahama, 1978), which are thought to have fractionated primarily at shallow levels (<4 km) (Platz et al., 2004). More olivine-rich compositions are thought to have crystallized in a magmatic reservoir at 10–14 km depth (Demant et al., 1994). The lithologies currently exposed at the main Nyiragongo crater are similar to the composition of the lava lake, and are feldspar-free, leucite-, melilite-, -nepheline-, oxide-, olivine-, and clinopyroxene-bearing foidites, with a markedly high concentration of LILE, high-field-strength elements (HFSE), and REE (Hertogen et al., 1985; Platz et al., 2004). The temperature at the surface of the lake has been measured to be approximately between ~500 (lake skin) and 1000 °C (Spampinato et al., 2013), whereas crater fountain temperatures are reported to approach 1100 °C (Sahama, 1978), which is the estimated liquidus temperature of the lava lake material (Tilley and Thompson, 1972). Conversely, the parasitic cones surrounding the volcano erupt olivine-melilite basalts (e.g., Demant et al. 1994; Platz et al. 2004; Barette et al. 2017), with a maximum reported alkali content of ~7 wt%, and a silica content below 41 wt% (Barette et al., 2017). Olivine, spinel, clinopyroxene, and melilite are the only minerals present in these lithologies (Demant et al., 1994; Platz et al., 2004).

3. Materials and methods

3.1. Sampling strategy and starting materials

Nine rock samples from the Nyiragongo volcano were used as starting materials for high-temperature experiments (Table 1; Fig. 1). Samples were collected during an expedition to the safely accessible south flank of the volcano organized in the summer of 2017. Samples for this study were selected to represent the full range of compositions from Nyiragongo. Compositions A, B, C, and N were collected from the main cone and selected for their large proportions of leucite (A), melilite (B), and nepheline (C and N). Compositions D, E, F, G, and H were collected from the parasitic cones surrounding the main edifice (Table 1; Fig. 1) and selected for being rich in clinopyroxene (D) and olivine (E, F, G, and H). Compositions A to D and N will be referred to as the low-Mg group (2.09–6.37 wt% MgO), whereas compositions E-H will be referred

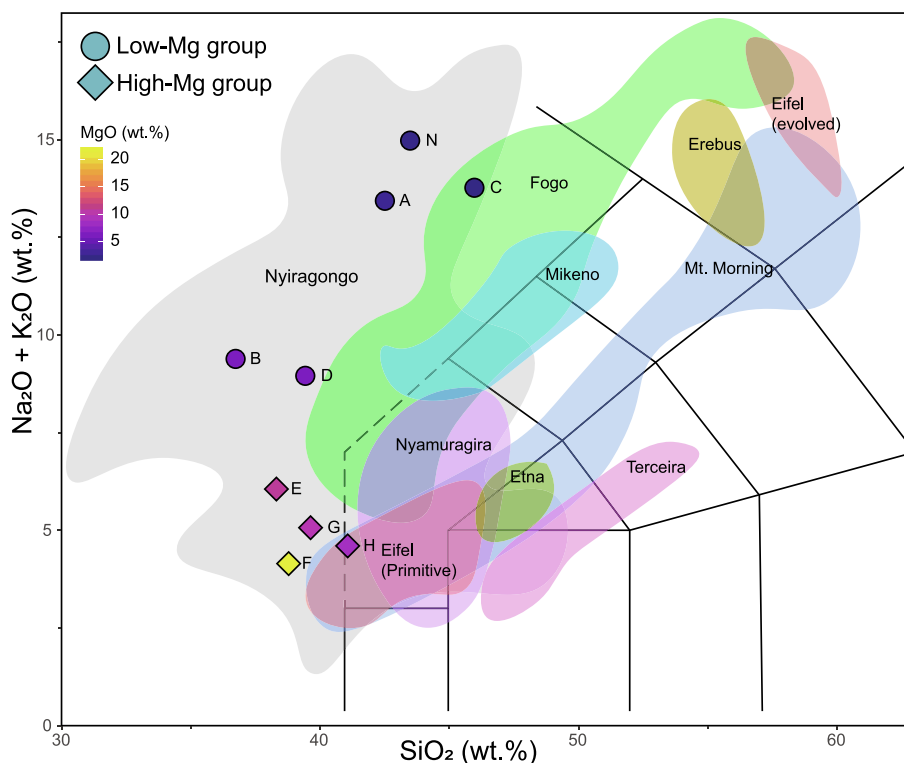


Fig. 1. Total Alkali-Silica (TAS) diagram including the starting compositions used for all experiments. Representative fields of various alkaline magmatic systems are included, with data of Nyiragongo, Mikeno and Nyamuragira (Barette et al., 2017), Pico do Fogo (Hildner et al., 2012; Eisele et al., 2015), the Eifel (Jung et al., 2006; Tomlinson et al., 2020), Etna (Viccaro et al., 2015), Terceira (Mungall and Martin, 1995; Regenauer-Lieb et al., 2015), Mount Morning (Martin et al., 2013), and Mount Erebus (Caldwell and Kyle, 1994; Iverson et al., 2014).

to as the high-Mg group (8.61–21.63 wt% MgO). This grouping reflects which samples were run together during each experiment, due to similarity in MgO and alkali content and, by extension, expected liquidus temperatures (Table 1). Thirty to 50 g of each sample were finely powdered at KU Leuven, Belgium. The major element composition of the powders was measured on lithium-metaborate fused glass discs at the University of Liège using an ARL PERFORM-X 4200 XRF (Table 1). Samples were dissolved using HF at Utrecht University, Netherlands, after which trace element contents were analysed using a PerkinElmer NexION 2000P ICP-MS (Table 1). Additional details on the XRF and ICP-MS whole-rock analytical methods are included in Supplementary Material 2.

3.2. Experimental techniques

Experiments were performed at one atmosphere in a GERO HTRV 70–250/18 gas-mixing furnace at the University of Liège, Belgium. Natural rock samples were ground to below 1 μm grain size using a Pulverisette planetary micro mill. Powders were subsequently homogenized in a Pulverisette 2 mortar grinder. Experimental runs were performed with oxygen fugacity (f_{O_2}) buffered at either QFM (quartz-fayalite-magnetite equilibrium) or QFM + 1. We used 0.2 mm diameter platinum loops annealed with 10–12 wt% Fe for QFM or 7–9 wt% Fe for QFM + 1, added by electroplating in order to mitigate for iron-loss during experimental runs (Grove, 1981). Loops were subsequently kept at 1300 $^{\circ}\text{C}$ in the furnace flushed with forming gas (95% N_2 , 5% H_2) for 72 h to facilitate iron diffusion into the platinum. All low-Mg group compositions were found to be super-liquidus at 1180 $^{\circ}\text{C}$, whereas the high-Mg group compositions were only super-liquidus above 1500 $^{\circ}\text{C}$. Powdered samples for all subsequent experiments were mounted on the loops and pre-heated in a muffle-furnace to

super-liquidus temperatures (1180 $^{\circ}\text{C}$ for low-Mg, 1500 $^{\circ}\text{C}$ for high-Mg group) for 2 min to make them homogeneous. Such a short run over the liquidus is not expected to hamper nucleation (Pupier et al., 2008). Samples were placed into the hotspot of the furnace ($\Delta T_{\text{gradient}} < 1$ $^{\circ}\text{C}$ over 5 cm) alongside a calibrated Pt₉₀-Rh₁₀ S-type thermocouple. Oxygen fugacity in the alumina tube was controlled by a mixture of high-purity CO and CO₂ gas introduced at the bottom of the furnace. Accuracy was checked with a SiRO₂ yttria-stabilized zirconia oxygen sensor.

Samples were initially kept at super-liquidus conditions (same as muffle furnace) for 2 h, a sufficient time to ensure f_{O_2} equilibration without affecting nucleation (Pupier et al., 2008). After 2 h, the temperature was dropped with a constant cooling rate of 2–3 $^{\circ}\text{C}/\text{h}$ (below that of the near-equilibrium cooling rate of Lofgren et al. (2006)) in order to ensure formation of large enough crystals for LA-ICP-MS analysis. Once these experiments reached the target temperature, they were left to equilibrate for 2 to 5 days depending on temperature (Table 2). Two super-liquidus quench experiments (NYA-2 and NYA-21) were also performed in order to evaluate alkali-loss during the pre-melt in the muffle furnace and the 2-hour super-liquidus stage in the gas-mixing furnace. No loss of alkalis was observed in these experiments. Losses observed in the larger set of experiments are listed in Table 2.

3.3. Electron microprobe analysis

Electron microprobe analysis (EMPA) of the experimental products was performed at Utrecht University, Netherlands, using a JEOL JXA-8530F Hyperprobe. Operating conditions were 15 kV for all analyses, using a beam current of 15 nA and 8–10 nA for crystals and glasses, respectively. A beam size of 10 μm was applied for both crystal and glass measurements in order to limit diffusion

Table 1

Major element oxide and trace element compositions of starting materials for the gas-mixing furnace experiments. MELTS liquidus estimates are reported for QFM conditions using Rhyolite-MELTS 1.0.2 (Gualda et al., 2012).

Grouping Sample name Lithology	Low-Mg group					High-Mg group			
	A Glomeroporphyritic Leucitite	B Melilitite	C Leucitite	D Pyroxene- Nephelinite	N Nephelinite	E Olivine- Melilite	F Olivine- Melilite	G Olivine- Melilite	H Olivine- Melilite
MELTS liquidus (°C)	1236	1475	1233	1182	1198	1221	1558	1201	1184
wt%									
SiO ₂	42.50	36.73	45.96	39.43	43.48	38.31	38.78	39.63	41.06
TiO ₂	2.18	2.85	1.43	3.25	1.53	3.14	1.86	3.53	3.39
Al ₂ O ₃	19.23	12.78	20.66	15.06	23.41	10.47	8.07	11.47	12.25
Fe ₂ O ₃	10.57	12.47	9.18	13.86	7.95	12.75	11.43	13.83	13.05
MnO	0.21	0.29	0.22	0.27	0.18	0.22	0.20	0.22	0.20
MgO	2.91	6.37	2.09	4.94	2.30	10.73	21.63	10.00	8.61
CaO	8.03	17.39	6.02	12.58	6.53	16.08	13.65	15.28	15.06
Na ₂ O	5.87	5.04	6.82	4.41	8.50	2.99	2.36	2.56	2.25
K ₂ O	7.56	4.35	6.95	4.55	6.48	3.06	1.79	2.50	2.35
P ₂ O ₅	1.35	1.97	0.75	1.83	0.81	1.46	1.05	1.03	0.75
LOI	0.63	0.00	1.29	-0.22	1.28	-0.23	-0.30	0.50	0.32
Total	101.05	100.24	101.37	99.96	102.44	98.97	100.52	100.56	99.30
ppm									
Sc	2.4	12.7	1.6	5.6	2.1	23.6	27	28.5	34.5
V	186	384	49.2	318	117	392	236	405	338.7
Cr	b.d.l.	16.4	b.d.l.	b.d.l.	b.d.l.	388	1227	177	188.7
Co	30.6	36.1	18.6	42.4	19.3	55.9	74.2	51.8	48.1
Ni	21.0	47.4	2.5	25.0	11.1	189.7	701.7	144.5	105.6
Cu	96.5	65.0	13.4	156.1	37.6	100.4	67.5	68.5	69.3
Zn	82.6	91.1	98.4	107.9	77.8	82.8	64.9	84.9	81.5
Rb	294.6	83.7	254.7	112.2	166.5	81.0	43.4	73.7	66.0
Sr	2243	3380	2753	2619	3099	2200	1649	1346	1253.7
Y	27.9	41.2	29.0	35.4	24.3	28.3	22.8	26.9	24.8
Zr	245	345	275	329	229	267	181	280	248.0
Nb	144.6	226.3	231.1	152.5	185.3	114.5	80.8	95.9	79.6
Mo	4.2	1.5	4.4	3.2	5.6	2.7	3.0	2.4	2.0
Cs	4.9	0.70	2.8	1.3	1.7	0.73	0.44	0.74	0.7
Ba	2478	2480	3047	2155	2899	1230	832	1334	1414.1
La	180	281	208	170	199	119	97	102	87.3
Ce	331	518	366	332	347	240	187	207	184.5
Pr	33	50	34	35	33	27	20	23	19.6
Nd	113	174	112	133	110	102	75	88	77.8
Sm	16	25	15	20	15	16	12	14	12.5
Eu	4.4	6.8	4.3	5.5	4.3	4.4	3.2	3.9	3.5
Gd	11	18	10	15	11	12	8.9	11	9.8
Tb	1.3	2.0	1.2	1.7	1.2	1.3	1.0	1.3	1.2
Dy	6.4	9.8	6.1	8.6	5.9	6.3	5.0	6.4	6.2
Ho	1.1	1.7	1.1	1.5	1.1	1.0	0.84	1.1	1.1
Er	3.0	4.5	3.2	3.9	3.0	2.7	2.2	2.8	2.8
Tm	0.38	0.56	0.44	0.48	0.39	0.32	0.27	0.34	0.4
Yb	2.4	3.4	2.9	3.0	2.5	1.9	1.6	2.1	2.2
Lu	0.35	0.50	0.42	0.42	0.37	0.28	0.23	0.30	0.3
Hf	3.7	5.9	4.0	6.1	4.0	5.6	4	7.4	7.1
Ta	45	54	26	16	24	4	10	12	12.9
W	3.0	1.3	2.9	1.7	1.9	1.4	1.5	1.4	1.5
Pb	1.7	5.8	5.2	4.2	5.4	2.7	3.8	2.6	1.8
Th	18	28	24	14	29	9.6	7.6	8.7	8.1
U	6.3	15	10	5.2	16	4.0	2.8	3.7	2.3

of alkali-metals. On-peak counting times of 20 s were employed for all elements, with off-peak (background) counting times of 10 s. Na and K were measured first in order to minimize the effect of alkali-loss. Primary standardization was performed using Smithsonian VG-2 (Si, Al for glasses; NMNH 111240-52) and in-house diopside (Si, Mg, Ca), corundum (Al), synthetic TiO (Ti), hematite (Fe), synthetic KTiPO₅ (P, K), celestine (Sr), jadeite (Na), barite (Ba) and tephroite (Mn). Secondary standardization was performed on Smithsonian VG-2 and A-99 basaltic glasses (NMNH 111240-52 and NMNH 113498-1, respectively), Kakanui augite (NMNH 122142), San Carlos olivine (NMNH 111312-44), ilmenite (NMNH 96189), and microcline (NMNH 143966). Relative errors on major element concentrations (based on secondary standards) were generally <5% for concentrations above 0.1 wt%. Specifically, relative

errors for minerals and glasses were up to 1.1% and 0.2% for SiO₂, 3.0% and 0.5% for Al₂O₃, 7.0% and 0.9% for MgO, 10.4% and 2.8% for TiO₂, 3.6% and 1.1% for FeO, 1.5% and 0.1% for CaO, 7.7% and 3.5% for Na₂O, 0.4% and 3.5% for K₂O, and 6.1% and 4.2% for MnO at these concentrations. P₂O₅ was only measured in glasses with a substantially higher error of 30%, attributed to their low concentrations (<0.38 wt%).

3.4. Laser-ablation mass spectrometry analysis

LA-ICP-MS analyses of experiments up to NYA-15 were performed at the ALIPP6 facility (Institut des Sciences de la Terre de Paris; Sorbonne Université, France) using an Analyte G2 UV excimer laser ablation system (wavelength of 193 nm) in parallel with

Table 2

List of experiments analysed by EMPA and LA-ICPMS. A full table including experiments analysed by EMPA but rejected for LA-ICPMS are listed in Supplementary Material 1. Numbers in brackets for run products, including glass (Gl), are volume percentages. Sodium and potassium losses are in percentage relative to the glass compositions from super-liquidus experimental runs 2 and 21, with the exception of composition N, for which XRF data was used.

Run	Composition	T _{pre-melt} (°C)	T _{Eq} (°C)	Equilibration time (h)	Cooling rate (°C/h)	ΔQFM	log fO ₂	Run products	Na-loss (% of start)	K-loss (% of start)
NYA-4	A	1200	1100	45.5	3.00	±1	-8.66	Lc (12), Ox (4), Gl (84)	6.18	4.87
NYA-7	A	1180	1050	68	3.00	±1	-9.36	Cpx (10), Lc (19), Neph (5), Ox (6), Rh (<1), Gl (60)	n.d.	n.d.
	B							Mel (34), Ox (10), Wh (<1), Gl (56)	n.d.	n.d.
NYA-8	A	1180	1075	60	3.00	±0.8	-9.22	Lc (17), Ox (5), Gl (78)	n.d.	n.d.
	B							Mel (27), Neph (<1), Ox (7), Gl (66)	n.d.	n.d.
	C							Lc (9), Ox (2), Gl (89)	n.d.	0.73
	D							Cpx (19), Lc (7), Ox (5), Rh (3), Gl (66)	3.54	3.39
NYA-9	A	1180	1025	82.35	3.00	±1	-9.72	Cpx (23), Lc (24), Neph (14), Ox (6), Gl (33)	n.d.	1.81
	B							Cpx (17), Mel (42), Neph (12), Ox (11), Rh (<1), Wh (<1), Gl (20)	5.80	6.37
	C							Cpx (4), Lc (17), Ox (4), Gl (75)	n.d.	n.d.
	D							Cpx (43), Neph (7), Ox (8), Wh (<1), Gl (42)	7.08	13.11
NYA-10	A	1180	1050	73	3.00	±1	-9.36	Cpx (<1), Lc (20), Rh (7), Ox (4), Gl (69)	n.d.	n.d.
	B							Cpx (13), Mel (36), Neph (13), Ox (9), Gl (29)	n.d.	19.38
	C							Lc (12), Ox (2), Rh (5), Gl (81)	n.d.	n.d.
	D							Cpx (32), Lc (9), Ox (7), Wh (2), Gl (50)	n.d.	22.82
NYA-11	A	1180	1075	75	3.00	±0	-10.01	Lc (15), Ox (3), Gl (82)	10.07	3.48
	B							Mel (30), Neph (7), Ol (2), Ox (7), Gl (54)	n.d.	n.d.
NYA-15	A	1180	1075	163	2.00	±0.8	-9.22	Lc (17), Ox (5), Gl (78)	n.d.	n.d.
	B							Mel (28), Neph (<1), Ox (7), Gl (65)	n.d.	n.d.
	C							Lc (9), Ox (2), Gl (89)	0.89	n.d.
	D							Cpx (21), Lc (7), Ox (6), Gl (66)	3.76	2.71
NYA-16	A	1180	1100		2.00	±0	-9.66	Lc (14), Ox (2), Gl (84)	1.24	n.d.
	B							Mel (16), Ox (2), Gl (82)	n.d.	n.d.
	C							Lc (10), Neph (4), Gl (86)	3.54	n.d.
NYA-17	E	1500	1200	70	2.00	±0	-8.41	Ol (8), Gl (92)	56.23	61.02
NYA-18	A	1180	1075	89	2.00	±0	-10.01	Lc (15), Ox (4), Gl (81)	2.12	n.d.
	B							Mel (26), Ol (1), Ox (7), Gl (66)	n.d.	n.d.
	D							Cpx (23), Lc (4), Ox (6), Gl (67)	n.d.	n.d.
NYA-19	A	1180	1050		2.00	±0	-10.36	Cpx (7), Lc (18), Ox (6), Gl (69)	n.d.	n.d.
	B							Mel (34), Neph (9), Ox (6), Rh (10), Gl (41)	n.d.	n.d.
	C							Lc (17), Ox (2), Gl (81)	9.89	n.d.
	D							Cpx (32), Lc (8), Ox (6), Gl (52)	n.d.	1.58
NYA-20	B	1180	1025	84	2.00	±0	-10.72	Mel (40), Neph (8), Ox (7), Rh (13), Wh (<1), Gl (32)	n.d.	n.d.
	C							Cpx (2), Lc (19), Ox (2), Rh (1), Gl (76)	2.36	n.d.
	D							Cpx (39), Ox (7), Rh (<1), Wh (3), Gl (50)	10.62	4.52
NYA-22	A	1180	1050	96	2.00	±0	-10.36	Mel (37), Neph (1), Ox (7), Rh (9), Gl (46)	4.59	1.11
	N							Cpx (1), Neph (30), Lc (7), Ox (<1), Rh (5), Gl (57)	2.83	3.09

an Agilent 8800 ICP-MS/MS. Data were acquired with 30 s of ablation, preceded and followed by gas background measurements. We used a pulse repetition rate of 8 Hz at an energy density of 2.48 J cm⁻². A beam diameter of 85 μm was applied for standards, melts and large crystals; for small crystals (primarily rhönite) the beam diameter was reduced down to a minimum of 25 μm. External standardization was performed using glass reference material NIST SRM 612, and performance evaluations were carried out using measurements of standards BIR-1G, BHVO-2G, ATHO-G, and BCR-2G. Mean relative errors of analysis were estimated to be <10% for concentrations of >1 ppm, and <20% for concentrations of <1 ppm. Analyses of experiments NYA-16 to NYA-22 were performed at Utrecht University, Netherlands using a ThermoFisher Scientific Element 2 magnetic sector ICP-MS connected to a Geolas 193 nm excimer laser, with a pulse repetition rate of 8 Hz, energy density of 2.7 J cm⁻², and a beam diameter of 60 μm. External standardization was performed using BCR-2G, and an identical set of standards to those used at ALIPP6 was used for performance evaluation (barring BCR-2G), resulting in relative errors of <15% for transition and post-transition metals (Zn and Pb, primarily), and <10% for other elements. Laser spots were placed at the rims of crystals when crystal size allowed for it, in all other cases the core was partially ablated. All resulting data were filtered to remove the potential influence of inclusions which were easily spotted by the presence of concentration peaks for some elements in measurement spectra.

3.5. Fitting approach

Blundy and Wood (1994) have described the relationship between the partition coefficient (D_i) of a cation with valence n in a given crystallographic site M with radius $r_{0(M)}^{n+}$ (in meters*10⁻¹⁰) and elastic modulus $E_{(M)}^{n+}$ (in Pascals*10⁹; GPa) can be described by the lattice strain model (see also Blundy and Wood, 1994; Blundy and Wood, 2003; Wood and Blundy, 2014), following the equation:

$$D_i = D_{0(M)}^{n+} * \exp \left\{ \frac{-4\pi N_A E_{(M)}^{n+} \left[\frac{1}{2} r_{0(M)}^{n+} (r_i - r_{0(M)}^{n+})^2 + \frac{1}{3} (r_i - r_{0(M)}^{n+})^3 \right]}{RT} \right\}$$

where N_A is Avogadro's Number, and $D_{0(M)}^{n+}$ is the strain-compensated partition coefficient of a cation of valence n and radius $r_{0(M)}^{n+}$. This equation has been used to approximate the parameters $r_{0(M)}^{n+}$, $E_{(M)}^{n+}$, and $D_{0(M)}^{n+}$ through a best-fit approach using measured Nernst partition coefficients, essentially constructing best-fit Onuma diagrams (Onuma et al., 1968) for cations of a given valence in their crystallographic site (e.g., Dalou et al. 2018). However the lattice strain model has been criticized for its erroneous description of the physics behind trace element incorporation into crystals and for mistakes in the derivation of the governing equation (Karato, 2016; Dubacq and Plunder, 2018). In particular, elastic parameters retrieved from fitting partition coefficients with the equations of (Blundy and Wood, 1994, 2003) have little physical meaning. Nevertheless, the lattice strain model was used in this study for its practical applications and due to the complexity of currently available alternatives limited to description of partitioning between melts or between crystals (e.g., Wagner et al., 2017; Figowy et al., 2020). The fitting procedure was based on a Monte-Carlo approach using 1 million randomly generated parameters within a given range (0.1–50 for $D_{0(M)}^{n+}$, 0–2500 GPa for $E_{(M)}^{n+}$). Lattice sites for specific elements were determined based on evaluation of D -value trends with cation size in relation to the nearest known major element cation sites. Effective ionic radii were derived from Shannon

(1976) and Jia (1991) and the $r_{0(M)}^{n+}$ range was set per valence and site, limited by the largest and smallest cations in consideration. Because both sites in leucite only have data on one side of their strain parabola, r_0 of this mineral was set to a fixed 1.9 Å for the W-site, and 0.39 Å for the T-site, corresponding to the ideal size of the W-site (Fabbrizio et al., 2008) and size of tetrahedrally coordinated Al³⁺, respectively. For each simulation, the quality of the fit was estimated using a chi-squared (χ^2) test, after which the best fit was stored. This procedure was repeated 100 times using D values falling within the 1 σ range for each element. The mean parameter values among the 100 best fit simulations were reported with an error defined as the 1 σ value of the remaining best ranked simulations for each parameter.

In order to compare experimental results with natural glass-crystal pairs, we also applied our model to literature data. When no temperature was reported, a temperature of 1000 °C was applied, in accordance with the approximate Nyiragongo lava lake temperature (Sahama, 1978).

4. Results

4.1. Crystallinity and equilibrium of run products

Fifty-five run products were characterised for major elements and were used to constrain phase equilibria. Out of those, only thirty-six were characterized for trace element partitioning. This is because: (1) eight products were not measured because they were run at super-liquidus conditions (Table 2; Fig. 3; 4); (2) five experimental products showed insufficient crystal size for laser ablation analysis, and four experimental products showed textural evidence for disequilibrium (e.g., unavoidable significant core-rim zoning, evidence for multi-stage growth, dendritic crystal forms), or abundance of inclusions in crystals (Table 2). Produced glasses were clear and homogeneous, with pools of sufficient size for laser ablation analysis. For most experiments, crystals were distributed homogeneously. However, clustering was observed at sample edges and around the Pt wire. Mass-balance calculations indicate minimal Fe-loss (<0.5 wt%) to the Pt wire. No significant correlation between equilibration temperatures and alkali-loss was observed within the low-Mg group, but a 5–10% difference was frequently observed between the calculated- (based on mass-balance) and initial alkali contents, as measured in the glasses of super-liquidus runs (Table 2). Experimental products varied in crystallinity between 2% and 80%, increasing steadily with decreasing equilibration temperature and the MgO content of the residual melt (Table 1; Fig. 3; 4).

4.2. Zoning features

Among the experimental run products, clinopyroxene and melilite show signs of zoning in the form of core-rim- and sector-zoning, respectively. Clinopyroxene core-rim zoning formed < 10 μm rims that showed a consistent trend from a Mg-rich core to Fe-rich rims (Fig. 2f). This transition was accompanied by a slight decrease in Al³⁺ which replaces Si⁴⁺, interpreted as a result of the continuous evolution of the melt during slow crystallization. Such features are not uncommon in experimentally derived clinopyroxene (e.g., Dygert et al., 2014; Beard et al., 2019). Because the rims were too small for pure LA-ICP-MS measurement, we will refrain from further discussing divalent cation partitioning for clinopyroxene. Whereas trivalent and tetravalent cations were also moderately affected by these features, their concentrations varied within uncertainty limits of the LA-ICP-MS (when measured with a 20 μm spot), and will therefore be considered as equilibrated.

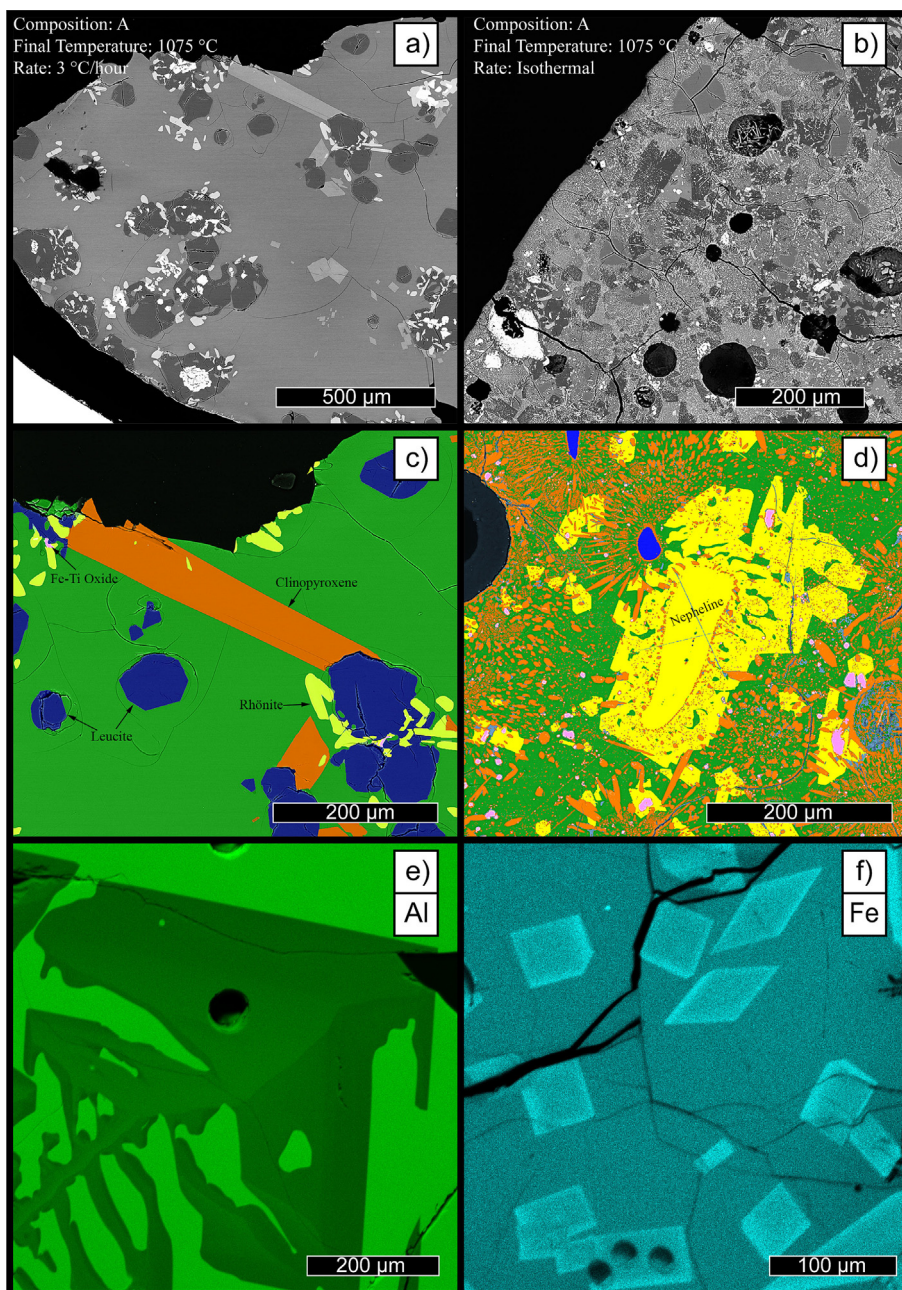
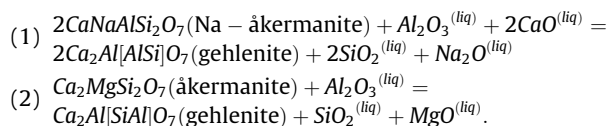


Fig. 2. Representative comparison between rate-cooled (a, c) and isothermal (b, d) experimental products, as well as EDX maps of reported zoning features (e, f). Images a-d are false colour BSE, with the colours red, blue, yellow, orange, and pink representing clinopyroxene, leucite, rhönite, nepheline, and spinel-structured oxide minerals. Melilite (e) and clinopyroxene (f) zoning features are displayed through Al-(e) and Fe-(f) EDX maps, respectively, showing sector (e) and core-rim (f) zoning features. (For interpretation of the references to colour in this figure legend, the reader is referred to the web version of this article.)

Melilite sector zoning was a consistent feature in our experimental products, similar to previously published literature (e.g., Lundstrom et al., 2006). Zoned crystals are divided into Al-rich and Al-poor domains (Fig. 2e). The Al-rich domains are poor in Mg^{2+} , Na^+ , and Si^{4+} , indicating that this Al^{3+} is introduced in both tetrahedral sites replacing Si^{4+} as well as Mg^{2+} , presumably through the following substitution mechanisms:



Such features have been previously reported in clinopyroxene, wherein the faster growing sections are less efficient in rejecting incompatible elements (Lofgren et al., 2006; Welsch et al., 2016). For this reason, the Al-enriched sections are filtered out in our results. Due to a general agreement of partitioning data with previously published work (see Section 5.1.2), we included the low-Al zone data.

4.3. Phase equilibria and glass compositions

Run products from experiments at QFM + 1 crystallized various combinations of leucite, nepheline, melilite, clinopyroxene,

spinel-structured oxides, rhönite, and Ca-phosphate minerals. Run products from experiments at QFM also included olivine (Table 2). Some samples which failed to produce crystalline Ca-phosphates instead showed spherical Ca-phosphate inclusions in late-crystallizing minerals. Crystals with such inclusions were excluded from trace element analysis, but their observation can help to explain phosphorous deficiencies in mass-balance calculations.

The five compositions of the low-Mg group (Fig. 3) developed differently with temperature, which resulted in differences in mineral assemblages. However, an overall trend of increasing melt Na₂O with differentiation was observed (Fig. 3e), coupled with decreasing FeO (Fig. 3b). Iron speciation in the glass was calculated using the approach of Putirka (2016) for use in the calculation of Fe²⁺-Mg exchange K_D values. Experiments on the high-Mg compositions were performed at only two temperatures, limiting discussion of major element trends, especially since these runs only

contained olivine and melilite as crystalline products. Detailed compositional information on a per-experiment basis is provided in Supplementary Material 2.

Compositions A, B, C, D, and N: Descending in temperature from 1180 °C, all low-Mg compositions started by crystallizing oxides, as evidenced by a continuous decrease in FeO and MgO (Fig. 3b). The next crystallizing phase on the liquidus varied depending on composition, between leucite (Comp A, C, D), nepheline (Comp N), or melilite (Comp B). For compositions A, B, and C, these phases were observed to crystallize above 1100 °C (Fig. 3d; 3f), whereas for compositions D and N, feldspathoids started crystallizing between 1100 °C and 1075 °C (Fig. 3e; 3f). Experiments on composition B at QFM conditions formed olivine in this temperature interval. Descending further from 1075 °C to 1050 °C, clinopyroxene and (minor) nepheline crystallized from all compositions, with rhönite appearing in samples of compositions A, D, and N.

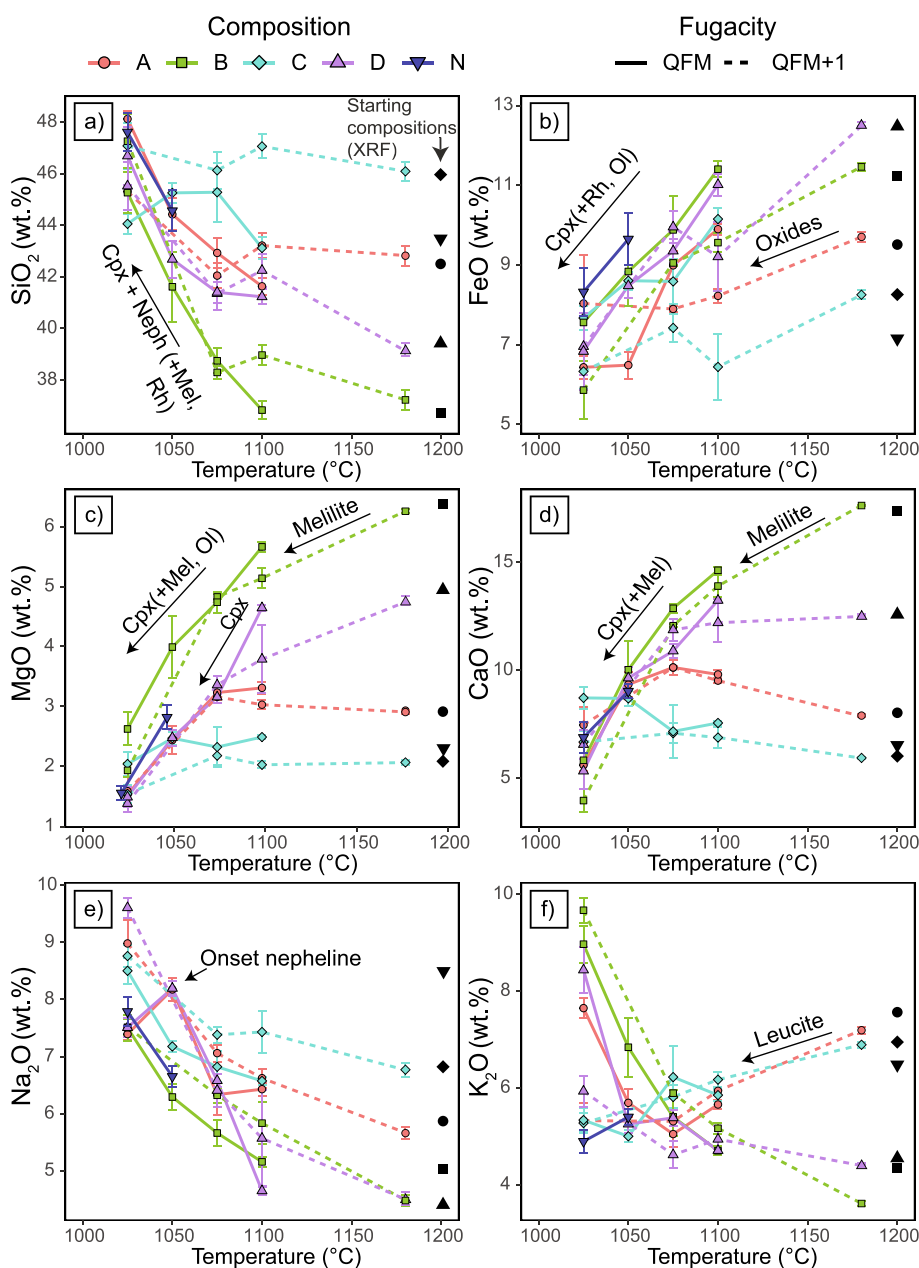


Fig. 3. Evolution of melt composition with equilibrium temperature for the low-Mg compositions A, B, C, D, and N. Key trends related to either crystallization of phases or alkali-loss are indicated.

Leucite stopped being the dominant crystallizing phase for compositions A and C at this temperature (Fig. 3f), and clinopyroxene formation dominated composition D samples below this temperature (Fig. 3d). In the final temperature interval from 1050 °C to 1025 °C, rhönite and Ca-bearing phosphates crystallized for all remaining compositions. Although having relatively similar liquidus temperatures, composition B was over 75% crystallized at this point, whereas composition C was still 75% melt, reflecting their contrasting chemistries and therefore crystallization paths.

Compositions E, F, G, and H: Between the liquidus (~1250–1500 °C; Table 1) and 1200 °C, the high-Mg group compositions only crystallized olivine, which generated an increase in all oxide-components other than MgO, FeO (which remained approximately stable), and the alkali oxides, the latter being related to alkali loss as opposed to crystallization (Fig. 4; Table 2). These trends were stronger for composition F, corresponding to its higher Mg# ($[\text{Mg}/(\text{Mg} + \text{Fe}^{2+})] * 100$) and liquidus.

4.4. Major element compositions of the minerals

Major element compositions of crystals are summarized below. A complete overview of representative compositions per experiment is provided in [Supplementary Material 1](#), and a more extensive discussion is listed in [Supplementary Material 2](#).

4.4.1. Leucite

Leucite was homogeneous between experiments, following the empirical formula of $\text{K}_{0.92}\text{Na}_{0.08}\text{AlSi}_2\text{O}_6$, similar to the average formula of $\text{K}_{0.94}\text{Na}_{0.06}\text{AlSi}_2\text{O}_6$ recorded by Platz (2002). Na substitution for K^+ (0.06–0.12 p.f.u.; 0.91–1.69 wt% Na_2O) in our compositions correlated with the Na^+ -concentration in the surrounding melt. Trace amounts of Fe^{3+} (assumed trivalent based on site filling approach; <0.03 p.f.u.; <1.01 wt% FeO) and Ca^{2+} (<0.01 p.f.u.; <0.22 wt% CaO) were also found.

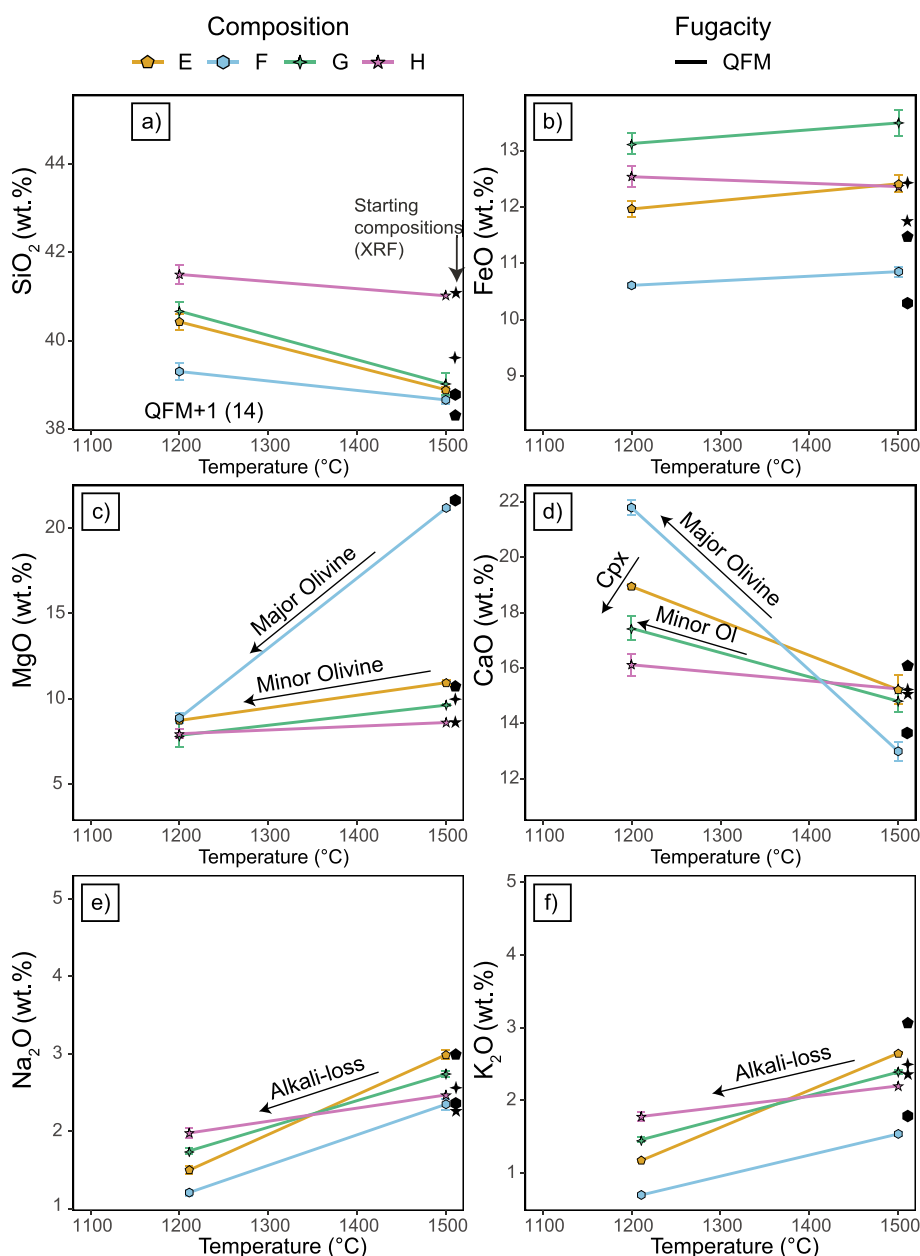


Fig. 4. Evolution of melt composition with equilibrium temperature for the high-Mg compositions E, F, G, and H. Key trends related to either crystallization of phases or alkali-loss are indicated.

4.4.2. Melilite

Melilite compositions were primarily Mg-rich aluoa kermanite [(Ca, Na)₂(Al, Mg, Fe²⁺)Si₂O₇] (Wiedenmann et al., 2009), including up to 10 mol% gehlenite (Ca₂Al₂SiO₇), and with increasing Na with differentiation from 0.22 Na p.f.u. (2.6 wt% Na₂O) at 1100  C, to 0.31 Na p.f.u. (3.6 wt% Na₂O) at 1025  C, with an outlier at 0.37 (4.2 wt% Na₂O) (Fig. S2, in Supplementary Material 2). The incorporation of Na⁺ can be explained by coupled exchange with Al³⁺ for Ca²⁺ and Mg²⁺, causing a trend towards Na- kermanite (CaNaAlSi₂O₇). All these compositions overlap with the compositional ranges reported by Platz et al. (2004) and Minissale et al. (2019) (see Figure S2).

4.4.3. Nepheline

The compositions of nepheline used for trace element analysis (experiment 22 N) followed the empirical formula [v_{0.3}K_{0.70}]Na_{2.7}Ca_{0.29}(Mg, Mn, Sr)_{0.01}[Fe_{0.1}Al_{3.95}Si_{3.95}]O₁₆ (where v represents a vacancy) based on a fixed 16 oxygen basis, reflecting a partially filled A site and minor Fe³⁺ in the T-site. High Ca-nepheline were also reported by Platz et al. (2004), who indicated up to 2.2 wt% CaO. Additional nepheline measurements from other experiments ranged in K-incorporation between 0.28 and 0.64, correlating negatively with the Na content of the melt.

4.4.4. Clinopyroxene

Clinopyroxene crystals were depleted in SiO₂ (37–45 wt%, 1.43–1.68 p.f.u.), which was compensated by ^{IV}Al³⁺- and Fe³⁺-enrichments (0.28–0.57 and 0.11–0.31 p.f.u., as calculated by the approach of Lindsley (1983)). The M1 and M2 sites are, in order of descending concentration per formula unit, filled with Ca²⁺ (0.90–0.96), Mg²⁺ (0.46–0.69), Fe^{2+/3+} (0.23–0.39), Ti⁴⁺ (0.06–0.20), ^{VI}Al³⁺ (<0.12), Na⁺ (0.03–0.07), and Mn²⁺ (<0.01), corresponding to Ca-, Mg-, and Al-rich diopside. These are diopside crystals richer in the CaTiAl₂O₆ and CaFe³⁺AlSiO₆ components than is traditionally reported in natural samples (Fig. S3a, in Supplementary Material 2), but similar compositions have been previously reported by Gee and Sack (1988).

4.4.5. Olivine

The forsterite content ($X_{Mg}^{ol}/(X_{Fe}^{ol} + X_{Mg}^{ol})$) of experimentally produced olivine varied between 0.77 and 0.91 (in agreement with the 0.82 to 0.89 range reported by Platz et al. (2004) for pyroxene nephelinites and alkali olivine basalts). The Fe-Mg partitioning between olivine and melt ($K_{DFe-Mg}^{ol-liq} = [(X_{Fe}^{ol} X_{Mg}^{liq}) / (X_{Mg}^{ol} X_{Fe}^{liq})]$) ranged from 0.21 to 0.26 and 0.25 to 0.27 for high- and low-Mg compositions, respectively.

4.4.6. Spinel-structured oxides

Oxide compositions were divided into ulv spinel, magnetite, and (Mg, Mn)(Al, Fe³⁺)₂O₄ spinel, varying primarily on the basis of melt composition but overlapping with the majority of published data on Nyiragongo volcanic rocks (Fig. S4, in Supplementary Material 2). The main compositional variation between samples occurred between magnetite-rich crystals in composition A, C, and D (27–55% Fe₃O₄, 17–36% Fe₂TiO₄, 21–42% Mg(Al, Fe³⁺)₂O₄) and the Mg-spinel-, and ulvospinel- rich crystals in composition B (8–34% Fe₃O₄, 22–46% Fe₂TiO₄, 29–53% (Mg, Mn)(Al, Fe³⁺)₂O₄).

4.4.7. Rh nite

Rh nite crystals were the primary Ti-rich phases produced, especially at low temperature (<1050  C). Their composition depended on the melt composition, with the main variability in the Fe, Mg, and Ti-bearing site. A compositional range was therefore observed between Mg-rich rh nite [(Ca_{1.8}Na_{0.2})(Mg_{3.0}Fe²⁺_{1.2}Fe³⁺_{0.8}Ti_{1.0})(Si_{3.4}Al_{2.3}Fe³⁺_{0.3})O₂₀], formed in composition B, and Fe-rich

rh nite [(Ca_{1.8}Na_{0.2})(Mg_{2.0}Fe²⁺_{1.4}Fe³⁺_{1.9}Ti_{0.7})(Si_{3.0}Al_{2.7}Fe³⁺_{0.3})O₂₀], of compositions A, C, D, and N.

4.5. Nernst partition coefficients

Crystal/melt partition coefficients are reported for 15 experimental products which produced inclusion-free crystals of sufficient size without disequilibrium features (see Section 4.1). A description of the trace element concentrations in minerals is given in Supplementary Material 2.

Minerals not considered for partition coefficients (oxides, Ca-phosphates) were not analysed for trace elements, and are not discussed further.

4.5.1. Leucite

Leucite readily incorporated significant amounts of the monovalent LILE Cs⁺ (D_{Cs} = 14.2–25.1) and Rb⁺ (D_{Rb} = 7.0–13.0), both of which are highly compatible, the degree of compatibility increasing with cation size (Fig. 5a). Following this trend, the partition coefficients of divalent Ba²⁺ and Sr²⁺ also positively correlated with cation size, ranging from incompatible Sr²⁺ (D_{Sr} = 0.01–0.05) to compatible Ba²⁺ (D_{Ba} = 0.78–2.06). In accordance with their smaller radius, divalent transition metals were found to be incompatible in leucite (Fig. 5a). The compatibility of all divalent cations increases with temperature.

Trivalent cations were highly incompatible in leucite, with the exception of near-compatible Cr³⁺ (D_{Cr} = 1.02–2.8). A trend of decreased compatibility with cation size was observed, indicating a slight preference for HREE over LREE (Fig. 5a). In an extension of the trend formed by HREE, Sc³⁺ is only weakly incompatible (D_{Sc} = 0.07–0.54).

Tetravalent and pentavalent high field-strength elements (HFSE) are incompatible in leucite (generally D < 0.01) (Fig. 5a). We observe some variation in these elements without a systematic relationship with temperature, especially Th and U, attributed to the extremely low concentrations in the mineral (generally < 0.01 ppm) closing in on the LA-ICP-MS detection limit.

4.5.2. Melilite

Monovalent cations were found to be incompatible in melilite, increasing in compatibility from Rb⁺ (D_{Rb} = 0.001–0.005) to Cs⁺ (D_{Cs} = 0.004–0.07). The same was true for divalent Ba²⁺ (D_{Ba} = 0.01–0.05), which was found to be slightly more compatible than Cs⁺ (Fig. 5b). In contrast, divalent Sr²⁺ (D_{Sr} = 1.2–2.5) and transition metals were found to be (near) compatible (Fig. 5b).

Trivalent cations were almost mildly incompatible in melilite, with the exception of near-compatible Cr³⁺ (D_{Cr} = 0.6–2.3). Lanthanides were found to decrease in compatibility from Eu³⁺ (D_{Eu} = 0.22–0.54) to Lu³⁺ (D_{Lu} = 0.03–0.08) (Fig. 5b), whereas the larger REE La³⁺ (D_{La} = 0.18–0.46) to Sm³⁺ (D_{Sm} = 0.19–0.48) all showed similar (moderately incompatible) partitioning behaviour, with compatibility correlating positively with the Na content of melilite.

Highly charged (4+, 5+) cations were incompatible in melilite (Fig. 5b), following a moderate positive correlation with temperature.

4.5.3. Nepheline

Nepheline was only measured by LA-ICP-MS in experimental products of composition N, due to small crystal sizes (<50  m in diameter) in other compositions. Mono- and divalent trace element cations were found to all be moderately incompatible (1 > D > 0.03) in nepheline. LILE decreased in compatibility with cation radius, and the mono-valent Rb⁺ (D_{Rb} = 0.68) and Cs⁺ (D_{Cs} = 0.28) were more compatible than the divalent Ba²⁺ (D_{Ba} = 0.06). Sr²⁺ (D_{Sr} = 0.37) is located near the peak of the divalent

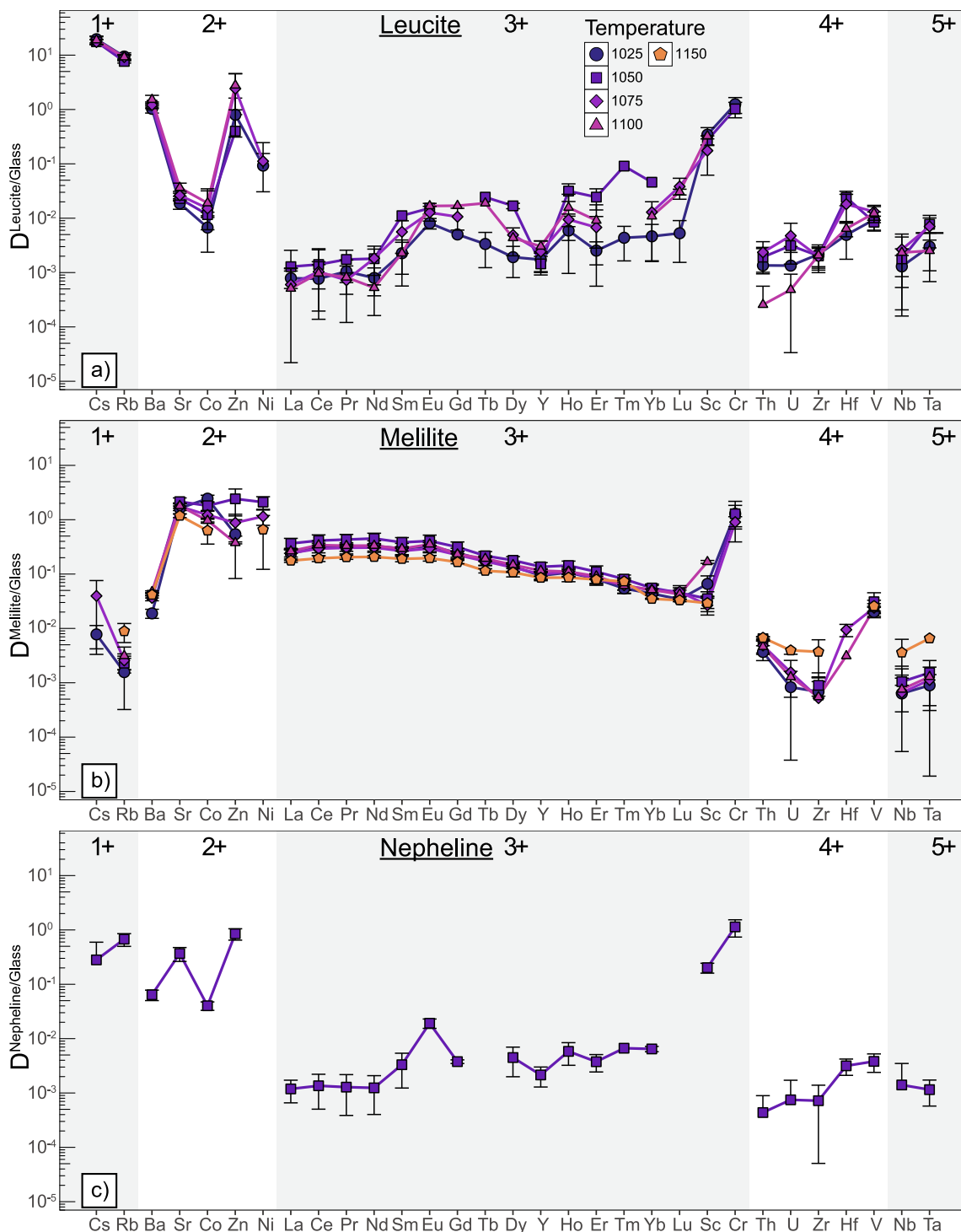


Fig. 5. Crystal-glass partition coefficients for (a) leucite, (b) melilite, and (c) nepheline. One standard deviation errors are displayed for each temperature measurement. Lower bound errors stretching below 10^{-5} are left out for clarity. For more details see Supplementary Material 1. Note that experiments above 1100 °C were performed with High-Mg starting compositions.

curve, slightly above D_{Cs} but less compatible than Rb^+ . Partitioning of trivalent cations in nepheline was characterized by a shallow upward slope from the highly incompatible LREE to HREE range, beyond which Sc^{3+} ($D_{Sc} = 0.20$) and Cr^{3+} ($D_{Cr} = 1.14$) appeared to be only moderately incompatible.

Tetra- and pentavalent cations were highly incompatible ($D < 0.01$) in nepheline (Fig. 5c), reflecting the lack of a suitable site for incorporation of these cations.

4.5.4. Clinopyroxene

Trace elements in clinopyroxene of low-Mg compositions could only be measured in composition D. The large monovalent cations Cs^+ ($D_{Cs} = 0.002-0.25$) and Rb^+ ($D_{Rb} < 0.02$) appeared to be highly incompatible (Fig. 6a) in clinopyroxene.

Partition coefficients of lanthanides increase from the largest cation La^{3+} ($D_{La} = 0.20-0.44$) up to intermediate Eu^{3+} ($D_{Eu} = 0.76-2.15$), beyond which partitioning decreased together with cation

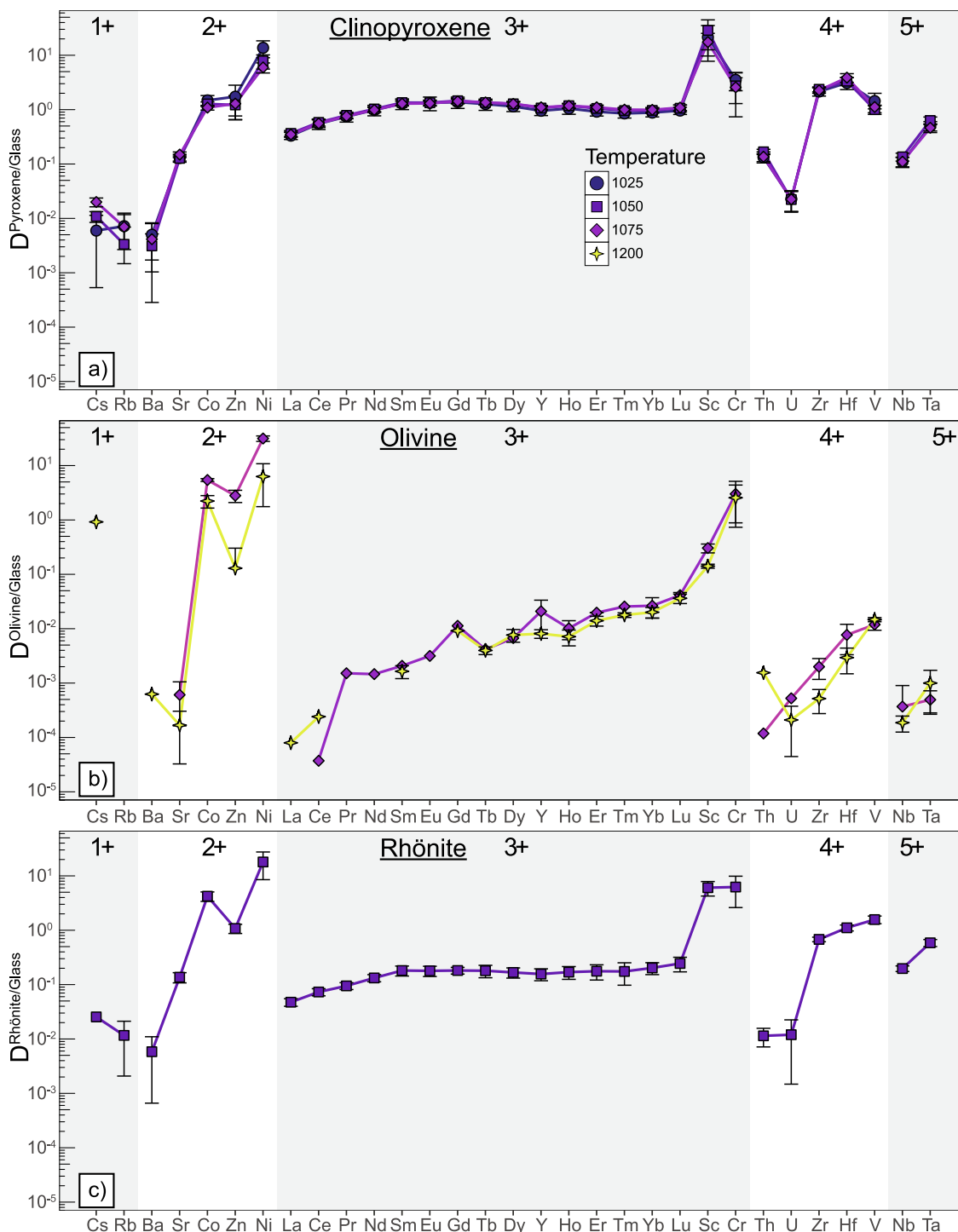


Fig. 6. Crystal-glass partition coefficients for (a) clinopyroxene, (b) olivine, and (c) rhönite. One standard deviation errors are displayed for each temperature measurement. Lower bound errors stretching below $1e^{-5}$ are left out for clarity. For more details see Supplementary Material 1. Note that experiments above $1100\text{ }^{\circ}\text{C}$ were performed with High-Mg starting compositions.

size following a shallow slope (Fig. 6a). Scandium was the most compatible ($D_{\text{Sc}} = 5.38\text{--}49.03$) trivalent cation in the clinopyroxene structure, approximately-one order of magnitude more compatible than the REE.

Among the HFSE, only Zr^{4+} ($D_{\text{Zr}} = 1.51\text{--}2.91$), Hf^{4+} ($D_{\text{Hf}} = 1.70\text{--}5.46$), and (at low temperatures) V^{4+} ($D_{\text{V}} = 0.61\text{--}2.65$) showed compatible behaviour (Fig. 6a). Thorium ($D_{\text{Th}} = 0.05\text{--}0.20$), U^{4+} ($D_{\text{U}} < 0.05$), and the pentavalent cations were found to be incompatible in clinopyroxene.

4.5.5. Olivine

The scarcity of olivine crystals produced in the experiments and the abundance of inclusions in the crystals resulted in limited trace element data, with less consistent results than for other silicates.

Monovalent cations in olivine were measured at concentrations close to the detection limits, highlighting their incompatibility but the data is insufficient for further discussion. Divalent transition metals were observed to be compatible, increasing from Co^{2+} ($D_{\text{Co}} = 1.64\text{--}5.74$) to Ni^{2+} ($D_{\text{Ni}} = 2.40\text{--}31.6$), and divalent LILE were highly incompatible (Fig. 6b).

In the range of trivalent cations, Cr^{3+} ($D_{\text{Cr}} = 0.36\text{--}5.39$) was found to have the highest partition coefficient, and is the only one above unit values, in an upward trend in partition coefficients starting at the highly incompatible La^{3+} ($D_{\text{La}} < 0.01$; Fig. 6b).

Partition coefficients of highly charged (4+, 5+) cations in olivine decrease with radius per valence (Fig. 6b), but remain highly incompatible (<0.01).

4.5.6. Rhönite

Despite its common occurrence, analysis of rhönite using LA-ICP-MS has proven difficult due to its elongated habit and commonly small crystal size ($<50\ \mu\text{m}$ width). Nevertheless, sizeable crystals from experiments 10A, 19B, and 22A provided consistent trace element patterns for 1050 °C (Fig. 6c) reminiscent of the structurally similar melilite and clinopyroxene.

LILE were found to be incompatible in rhönite, decreasing in compatibility in the order of Sr^{2+} ($D_{\text{Sr}} = 0.10\text{--}0.16$), Cs^+ ($D_{\text{Cs}} = 0.03$), Rb^{2+} ($D_{\text{Rb}} = 0.01\text{--}0.02$), and Ba^{2+} ($D_{\text{Ba}} < 0.01$). Divalent transition metals were instead found to be clearly compatible in rhönite (Fig. 6c).

Sc^{3+} ($D_{\text{Sc}} = 4.81\text{--}8.10$) and Cr^{3+} ($D_{\text{Cr}} = 2.69\text{--}10.2$) showed a high compatibility similar to divalent transition metals, plotting just below Ni^{2+} ($D_{\text{Ni}} = 9.94\text{--}26.1$). Lanthanides instead followed an increasing compatibility trend from La^{3+} ($D_{\text{La}} = 0.04\text{--}0.06$) to Sm^{3+} ($D_{\text{Sm}} = 0.15\text{--}0.23$), with a plateau of partition coefficients observed for Eu^{3+} ($D_{\text{Eu}} = 0.15\text{--}0.22$) to Lu^{3+} ($D_{\text{Lu}} = 0.19\text{--}0.33$).

Rhönite was found to contain abundant HFSE, with a particularly notable preference for the smaller ions Zr^{4+} ($D_{\text{Zr}} = 0.64\text{--}0.74$), Hf^{4+} ($D_{\text{Hf}} = 1.08\text{--}1.15$), V^{4+} ($D_{\text{V}} = 1.43\text{--}1.72$), Nb^{5+} ($D_{\text{Nb}} = 0.19\text{--}0.21$), and Ta^{5+} ($D_{\text{Ta}} = 0.55\text{--}0.68$), for which the partition coefficients were close to unity (Fig. 6c). The larger tetravalent cations Th^{4+} ($D_{\text{Th}} < 0.01$) and U^{4+} ($D_{\text{U}} < 0.02$) were found to be significantly less compatible, similar to monovalent cations.

5. Discussion

5.1. Lattice strain model

The partitioning behaviour for elements of each valence state in each mineral/melt pair was modelled using a lattice-strain fitting approach (Blundy and Wood 1994; see Section 2.5). Cations were distributed over the available crystallographic sites based on their radius and charge under the relevant $f\text{O}_2$ conditions. Fit parameters were then determined for every unique combination of experimental conditions (temperature, $f\text{O}_2$, composition) on a mineral-by-mineral basis, a summary of which can be found in Supplementary Material 1. Representative examples are discussed below.

5.1.1. Leucite [$\text{W}(\text{T})_3\text{O}_6$]

Leucite has two crystallographic sites in which substitution is viable: the distorted twelfold coordinated W-site occupied by K^+ , and the tetrahedral site normally occupied by Al^{3+} and Si^{4+} (Deer et al., 1966; Volfinger and Robert, 1980; Fabbriozio et al., 2008). The large ($>1.3\ \text{\AA}$) mono- and divalent cations occupy the larger W-site, whereas the more highly charged, smaller cations fall on parabolic curves consistent with partitioning into the T-site, together with Al^{3+} (Fig. 7). A notable exception to the distribution of cations per valence are the divalent transition metals, as well as Mg^{2+} , which form a scattered distribution in logD-cation radius space (here displayed with 4-fold coordination). This is a consequence of the lack of an energetically favourable site for these small divalent cation site, resulting in disordered distribution over the 4-fold site (Fabbriozio et al., 2008 and references therein). Highly compatible monovalent ions in the W-site define a curve which peaks just beyond Cs^+ ($r_{\text{Cs}}^{\text{III}} = 1.88\ \text{\AA}$). However, the true r_0

value for this site cannot be fitted due to a lack of data on the far side of the curve, and it is therefore fixed to $1.9\ \text{\AA}$. The $D_{0(\text{W})}^{1+}$ -value for our experiments varies between 13.3 and 19.1, with an $E_{0(\text{W})}^{1+}$ parameter fitted to 31.3–35.6 GPa. In line with the findings of Fabbriozio et al. (2008), the divalent W-site curve is shown directly under that of monovalent cations ($D_{0(\text{W})}^{2+} = 9.6\text{--}15.4$), with r_0 fixed to $1.9\ \text{\AA}$ once again. Outliers were observed for QFM experiments at 1100 °C, which plot significantly higher ($D_{0(\text{W})}^{2+} = 22.7\text{--}29.8$) on account of a lower D_{Ca} value which increases the slope of the lattice strain curve. Nevertheless, the $E_{0(\text{W})}^{2+}$ -value of divalent cations is uniformly limited to the range of 50.9–59.8 GPa. Despite REE commonly substituting for Ca^{2+} (e.g., pyroxene), which is mainly found in the W-site of leucite, trivalent cations show a pattern of T-site-incorporation (Fig. 7). As before, Onuma diagrams were fixed to peak at Al^{3+} ($r_{\text{Al}}^{\text{IV}} = 0.39\ \text{\AA}$) considered as the major host of the site. However, the consistently incompatible behaviour of trivalent cations in leucite means that $D_{0(\text{T})}^{3+}$ remains low (0.24–1.01). This curve has a higher fitted E_0 parameter ($E_{0(\text{T})}^{3+} = 98\text{--}173\ \text{GPa}$) than the W-site, highly influenced by $D_{\text{Sc}}^{\text{Leucite}}$. No Onuma curves are constructed for tetravalent cations.

The same best-fit lattice strain approach applied to previous studies (Francalanci et al., 1987; Ewart and Griffin, 1994; Wood and Trigila, 2001; Foley and Jenner, 2004; Fabbriozio et al., 2008; Minissale et al., 2019) reveals mostly similar results. Curves constructed from the data of Francalanci et al. (1987) were excluded due to anomalously low $D_{\text{Cs}}^{\text{Leucite}}$ (below $D_{\text{Rb}}^{\text{Leucite}}$ values hampering fitting). The other studies show monovalent partitioning curves in agreement with the present study, except for slight variations in $D_{0(\text{W})}^{1+}$ (Fig. 7). In particular, partition coefficients from Minissale et al. (2019) are high ($D_{0(\text{W})}^{1+} = 21.3\text{--}26.8$) compared to both natural and experimental studies from other alkaline systems (Wood and Trigila, 2001; Foley and Jenner, 2004; Fabbriozio et al., 2008), which provide $D_{0(\text{W})}^{1+}$ values between 7.1 and 13.0. This discrepancy reflects significantly higher D_{Rb} (11.0–11.1) and D_{Cs} (23.0–24.6) values in the former study, which may be explained through the higher $^{\text{W}}\text{K}/^{\text{W}}\text{Na}$ ratio in their leucite crystals leading to an, on average, larger site (a feature which cannot be evaluated here due to the lack of high-r constraints). A similar pattern is found for divalent cations, with the $D_{0(\text{W})}^{2+}$ values of Wood and Trigila (2001), Foley and Jenner (2004), and Fabbriozio et al. (2008) being significantly lower than those of Minissale et al. (2019) and our own (Fig. 7). However, this can be explained by an elevated D_{Ca} value in the latter studies, causing curve flattening despite comparable D_{Ba} and D_{Sr} values, and also explaining the difficulty fitting Ca reported by Fabbriozio et al. (2008). Despite a lack of complete sets of trivalent leucite partition coefficients, data of Fabbriozio et al. (2008), Foley and Jenner (2004), and Minissale et al. (2019) agree largely with our data. Measurements of tetravalent cations in leucite are limited to one sample from Minissale et al. (2019)'s, falling within error of our results.

5.1.2. Melilite [$\text{X}_2\text{T}1(\text{T}2)_2\text{O}_7$]

Substitution in melilite is possible in the eightfold coordinated X-site which hosts Ca^{2+} and Na^+ , the fourfold coordinated T1-site, which is occupied by Mg^{2+} , Fe^{2+} , Fe^{3+} , and Al^{3+} (Smyth and Bish, 1988; Bindi et al., 2001), and the similarly coordinated T2-site which hosts Si^{4+} and/or Al^{3+} . The inclusion of monovalent cations is only observed in the X-site forming a curve that peaks at radius slightly larger than Na^+ ($r_{\text{Na}}^{\text{III}} = 1.18\ \text{\AA}$, $x_{\text{r}_0}^{1+} = 1.23\text{--}1.27\ \text{\AA}$; Fig. 8). Despite Na^+ being a major component in the alumaöaker-

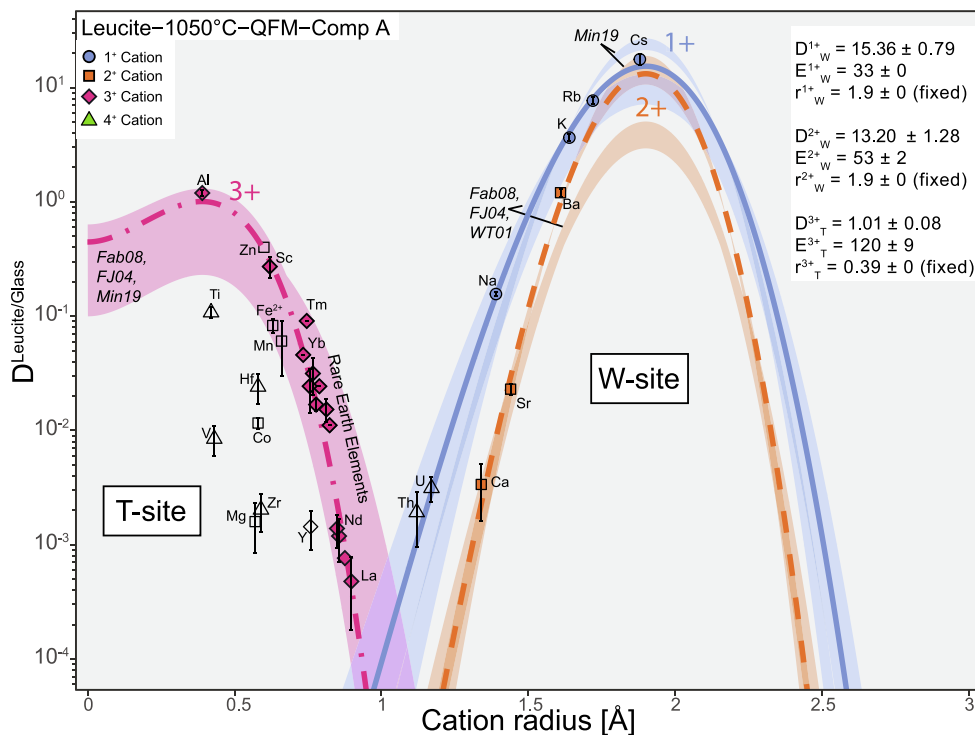
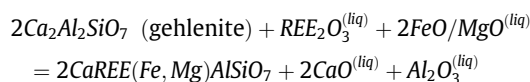


Fig. 7. Representative best-fit lattice strain curves for mono- to tetravalent ions in the leucite structure for a single set of conditions (listed top left). Ionic radii are for twelffold (1+, 2+) and fourfold (3+, 4+) coordination taken from Shannon (1976). Fourfold radii are in a large part acquired through extrapolation following the approach by Jia (1991), see Section 2.5. D_0 values are unit-less, E_0 values are in GPa, and r_0 values are listed in Å. Open symbols were not considered for the fitting approach. Shaded areas and/or lines represent literature data, whereas full opacity lines are from this study. This also applies for further figures. Abbreviations for sources of literature curves are as follows: Fab08: (Fabrizio et al., 2008), FJ04: (Foley and Jenner, 2004), Min19: (Minissale et al., 2019), WT01: (Wood and Trigila, 2001).

manite structure, partition coefficients for monovalent cations into this site are moderately low ($D_{0(X)}^{1+} = 0.53 - 0.71$). The site has a moderate fitted elastic modulus ($E_{0(X)}^{1+} = 77 - 107$ GPa). Divalent cations are distributed over the X- and T1-sites depending on size; with the T1 site incorporating Mg^{2+} and the transition metals, and the X-site incorporating the larger alkaline earth metals. T1-site incorporation of transition metals ($D_{0(T1)}^{2+} = 1.11 - 3.09$) peaks near Ni ($r_{Ni}^{2+} = 0.53 - 0.55$ Å; $r_{Ni}^{IV} = 0.55$ Å), but is subject to uncertainty resulting from the lack of smaller cations. Divalent cation incorporation into the X site represents the highest lying curve for melilite ($D_{0(X)}^{2+} = 4.07 - 4.95$), peaked by Ca^{2+} ($r_{Ca}^{VIII} = 1.12$ Å; $r_{Ca}^{2+} = 1.07 - 1.14$ Å), followed by decreasingly compatible Si^{2+} and Ba^{2+} . The X-site also hosts the trivalent lanthanide group, with a peak in D values between Pr^{3+} and Nd^{3+} ($D_{0(X)}^{3+} = 0.28 - 0.48$; $r_{0(X)}^{3+} = 1.11 - 1.12$ Å). Slightly elevated Al^{3+} concentrations, replacing divalent cations in the T1-sites in the Al-rich domains of zoned crystals promote the incorporation these elements through coupled substitution, but the corresponding concentration changes are of lower magnitude than inter-crystal variability combined with errors on LA-ICP-MS measurements. Trivalent cations in the T-sites are limited to Al^{3+} , Cr^{3+} , and Sc^{3+} . Tetravalent cation incorporation in melilite is scarce, with Th^{4+} and U^{4+} partitioning into the X-site, and Ti^{4+} , Hf^{4+} , and Zr^{4+} preferring the T-sites. The associated partitioning curves for the latter have a low $D_{0(T)}^{4+}$ (0.04–0.09), high elastic moduli ($E_{0(T)}^{4+} = 1172 - 1900$ GPa), and consistent $r_{0(T)}^{4+}$ of 0.46–0.47 Å.

A variety of authors have previously studied trace element partitioning into the melilite structure, some focusing on their presence in calcium-aluminium inclusions (CAIs) in chondritic meteorites (e.g., Beckett et al. 1990; Lundstrom et al. 2006;

Ustunisk et al. 2019), others carrying out measurements over natural or experimental igneous melilite (e.g Nagasawa et al. 1980; Onuma et al. 1981; Kuehner et al. 1989; Arzamastsev et al. 2009; Minissale et al. 2019). Application of the fitting approach to the available divalent data reveals an overall agreement with ours, especially with the data from natural samples of Minissale et al. (2019) (Fig. 8). X-site occupancy parameters for divalent cations are comparable between studies, except for $D_{0(X)}^{2+}$, which is noticeably lower (1.59–1.92) for the gehlenite-rich experimental products of Lundstrom et al. (2006) and Ustunisk et al. (2019). This is somewhat unexpected given that gehlenite requires a fully divalent X-site, and the feature is therefore attributed to the melt composition, given that both studies are performed on CAI melts as opposed to terrestrial ones. A similar pattern is observed for trivalent cation incorporation, wherein $D_{0(X)}^{3+}$ is significantly depressed (0.04–0.08) in the samples of Beckett et al. (1990), Kuehner et al. (1989), and Lundstrom et al. (2006). Conversely, REE partitioning in the gehlenite-rich samples of Ustunisk et al. (2019) appears elevated ($D_{0(X)}^{3+} = 1.26$), with a significantly smaller fitted elastic modulus ($E_{0(X)}^{3+} = 81$ GPa), which is better in line with current views on melilite REE-incorporation (Kuehner et al., 1989). Previous work by Beckett et al. (1990) linked the individual partitioning of LREE in melilite with the X_{geh}/X_{Ak} ratio, following the reaction:



Which indeed explains the high $D_{0(X)}^{3+}$ values reported by Ustunisk et al. (2019), but fails to explain the variations between åkermanite-rich compositions, since it does not take sodium into account, which may greatly affect the X-site of melilite by allowing

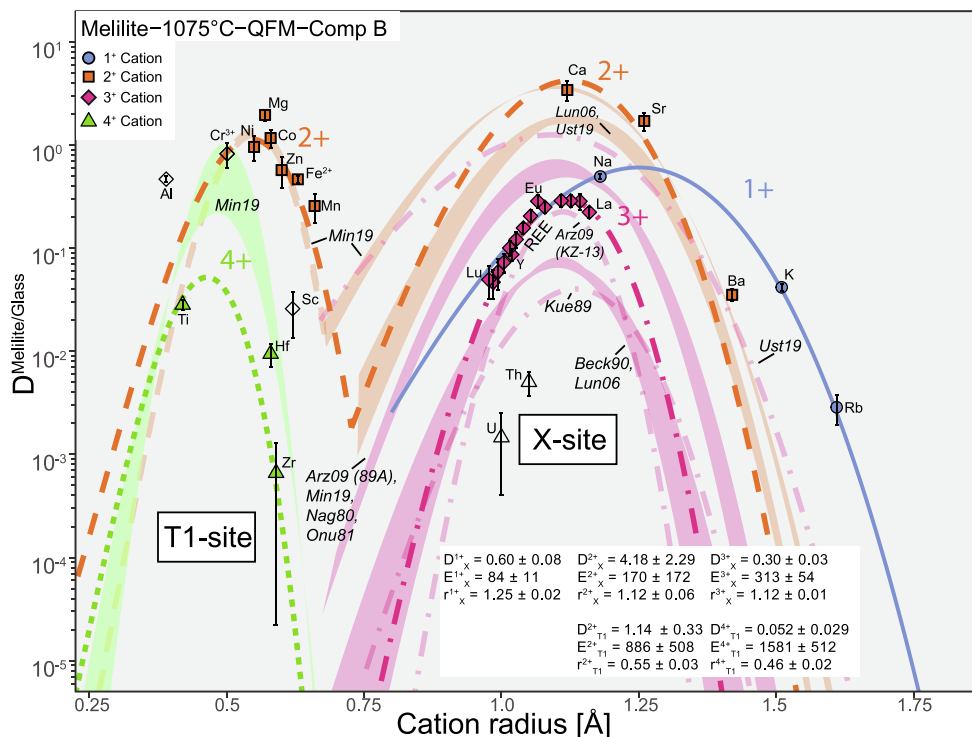


Fig. 8. Representative best-fit Onuma curves for mono- to tetravalent ions in the melilite structure for a single set of conditions (listed top left). Ionic radii are for four- (T1-site) and eightfold (X-site) coordination taken from Shannon (1976). Select fourfold radii are acquired through extrapolation following the approach by Jia (1991), see Section 2.5. Abbreviations for sources of literature curves are as follows: Arz09: (Arzamastsev et al., 2009), Beck90 (Beckett et al., 1990), Kue89: (Kuehner et al., 1989), Lun06: (Lundstrom et al., 2006), Min19: (Minissale et al., 2019), Nag80: (Nagasawa et al., 1980), Onu81: (Onuma et al., 1981), Ust19: (Ustunisik et al., 2019).

coupled substitution with Na. Instead, we observed that a combination of X_{Na} (increasing $E_{0(X)}^{3+}$), Al^T (decreasing $E_{0(X)}^{3+}$), and temperature (decreasing $D_{0(X)}^{3+}$) most adequately explains the differences between studies. The $E_{0(X)}^{3+}$ values reported by Minissale et al. (2019) are anomalously high for their crystal compositions, but this can be explained through large discrepancies in the heaviest HREE (Tm, Yb, and Lu; all reported at 0.1 ppm, likely close to the detection limit) which artificially flatten the strain curve.

Tetravalent substitution into the T-sites is consistent between our data and those of Minissale et al. (2019) in terms of site radius and high fitted elastic modulus ($E_{0(T)}^{4+} = 1572 - 2218$ GPa), but has a variable $D_{0(T)}^{4+}$ (0.22–1.03) on account of frequently being controlled by at most three cations.

5.1.3. Nepheline [$AB_3(T1-4)_8O_{16}$]

Aside from its four tetrahedral sites, nepheline comprises an eightfold coordinated B-site primarily occupied by Na^+ and a ninefold coordinated A-site occupied by K^+ , both of which may be subject to trace element substitution (Smyth and Bish, 1988; Tait et al., 2003; Antao and Nicholls, 2018). Dollase and Thomas (1978) described the A-site as only including either a vacancy or charge balancing K^+ (or Rb^+ , Cs^+) ion. Since we report partition coefficients from experiment 22 N only, lattice parameters are given as single values with associated error based on the fitting approach. As was the case for leucite, a lack of data for one side of the parabola complicates establishing the monovalent partitioning curve for nepheline. The obtained monovalent Onuma diagram forms a near-flat curve, with an elastic modulus ($E_{0(A)}^{1+}$) of 10 ± 4 GPa. The site's $r_{0(A/B)}^{1+}$ is larger than Na^+ ($r_{Na}^{VIII} = 1.18$ Å), at 1.21 ± 0.01 Å. Divalent cation incorporation is considered to occur primarily in the B-site. Lattice strain parabola indicate a similar optimal site radius to

monovalent incorporation, at 1.23 ± 0.01 Å. The fitted elastic modulus for divalent cations is significantly higher, at 88 ± 13 GPa. Whereas lanthanides may substitute in the same site as Ca^{2+} , their distribution in the Onuma diagram suggests an unrealistically low $r_{0(B)}^{3+}$ when using 8-fold coordination (Fig. 9). Instead, T-site incorporation appears likely, but the scarcity of the data prohibited constructing partitioning curves. Monovalent data from samples of Minissale et al. (2019) plot above our curve, but at a similar position (1.32–1.40 Å). Divalent cation fits are instead heavily influenced by their $\frac{D_{Ca}}{D_{Sr}}$ ratio, a high value of which (>0.8) (e.g., Dawson et al. (2008); this study) indicates an ideal site radius slightly smaller than r_{Sr}^{VIII} , whereas a low ratio (<0.6) such as observed for Larsen (1979) and Minissale et al. (2019) implies a larger crystal site (1.26–1.28 Å) despite a similar fitted elastic modulus ($E_{0(B)}^{2+} = 84 - 92$ GPa). No concrete controlling mechanism could be inferred due to scarcity of available studies.

Trivalent cations in nepheline have not been thoroughly reported. Larsen (1979) and Minissale et al. (2019) provide the only available complete data-sets of REE partition coefficients, the former of which reports phenocryst/whole-rock coefficients, and the latter phenocryst/glass partitioning. The data of Larsen (1979) is thoroughly clustered around $D^{3+} = 10^{-2}$ and lacks Sc^{3+} , and the data of Minissale et al. (2019) provides an image similar to that of our study, but with significantly higher partition coefficients for MREE to HREE (e.g., $D_{Yb} = 0.14$ vs our $6-7 \cdot 10^{-3}$). However, it is noteworthy that the nepheline REE data of Minissale et al. (2019) are scarce, and their HREE data are close to detection limits.

5.1.4. Clinopyroxene [$M2M1(T)_2O_6$]

Trace element substitution in clinopyroxene is well-documented to occur in the VI-coordinated M1 and VIII-coordinated M2 sites, (e.g., Wood and Blundy, 1997; Lundstrom

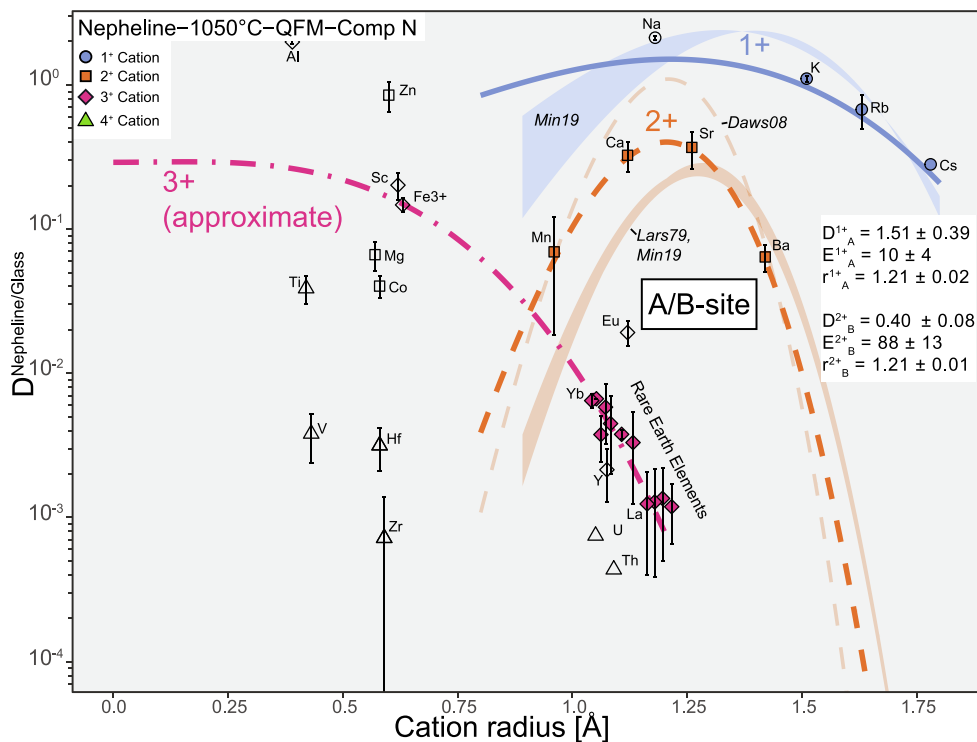


Fig. 9. Representative best-fit Onuma curves for mono- to tetravalent ions in the nepheline structure for a single set of conditions (listed top left). Ionic radii are for eight- (B-site), nine- (A-site), and four- (T-sites) fold coordination taken from Shannon (1976). Fourfold radii are in a large part acquired through extrapolation following the approach by Jia (1991), see Section 2.5. Abbreviations for sources of literature curves are as follows: Daws08: (Dawson et al., 2008), Lars79: (Larsen, 1979), Min19: (Minissale et al., 2019), Onu81: (Onuma et al., 1981).

et al., 1998; Neumann et al., 1999; Wood and Trigila, 2001; Hill et al., 2012; Mollo et al., 2016; Bonechi et al., 2021), the latter of which potentially incorporates the full range of REE. Monovalent cation partitioning data in this study are insufficient to construct meaningful Onuma curves, and are therefore excluded. Similarly, divalent partition coefficients are excluded for equilibrium reasons (see Section 4.2). Among trivalent cations Cr^{3+} and Sc^{3+} partition into the smaller M1 site, whereas the $\text{REE}^{3+} + \text{Y}^{3+}$ partition into M2, for which the ideal site radius is close to that of Gd^{3+} ($r_{0(M2)}^{3+} = 1.05 - 1.06 \text{ \AA}$). Lu^{3+} and Yb^{3+} are observed to diverge slightly from this curve, indicating minor incorporation into the M1-site. No M1-site parabola for this valence could be constructed on account of Cr^{3+} and Sc^{3+} being the only contributing cations. Trivalent M2-site Onuma curve E_0 -values decrease with temperature (287–331 GPa between 1025 and 1075 °C). M1-site tetravalent trace element incorporation is dictated by V^{4+} , Ti^{4+} , Hf^{4+} , and Zr^{4+} , which form a tight curve ($r_{0(M1)}^{4+} = 0.65 - 0.67 \text{ \AA}$; $E_{0(M1)}^{4+} = 1031 - 2060 \text{ GPa}$; $D_{0(M1)}^{4+} = 4.74 - 15.17$), whereas the M2-site curve is left out due to only being pinned by Th^{4+} and U^{4+} . The investigation of clinopyroxene in alkaline systems has recently received significant attention (e.g., Beard et al., 2019; Baudouin et al., 2020; Bonechi et al., 2021), allowing for more thorough comparison between studies. Nevertheless, the high degree of M1-site incorporation of HREE reported by the first two of these authors was not reproduced with our samples, which lack a significant aegirine component. Meaningful M1-site trivalent strain curves can be constructed for the data of Larsen (1979), Wood and Trigila (2001), Foley and Jenner (2004), Arzamastsev et al. (2009), Ambrosio and Azzone (2018), Beard et al. (2019), Minissale et al. (2019), and Baudouin et al. (2020), among which the data of Ambrosio and Azzone (2018) are in best agreement with our data (Fig. 10). The samples of Beard et al. (2019) and

Baudouin et al. (2020) display unusually high degrees of REE incorporation into the M1-site, a feature attributed to a decreasing electrostatic penalty at high aegirine contents (due to $^{\text{VI}}\text{Fe}^{3+}$), coinciding with a decreasing radius of the M1-site (Beard et al., 2019; Baudouin et al., 2020). Trivalent cation occupancy into the M2-site may consequently be negatively correlated with that of the M1-site since it performs a charge-compensating role. Nevertheless, data from the experiments of Beard et al. (2019) still produce significantly elevated M2-site partitioning curves for trivalent cations (Fig. 10). The same can be said for the data of Wood and Trigila (2001). Those of the remaining natural studies more often present comparative enrichment of REE in the melt compared to the crystal. Despite being compositionally unusual, our M2-partitioning data is in line with previous observations of a link between increased D -values and tetrahedral aluminium (e.g., Hill et al., 2000; Wood and Trigila, 2001; Sun and Liang, 2012), but needs to be adjusted for silica-undersaturated cpx-components ($\text{CaTiAl}_2\text{O}_6$ and $\text{CaFe}^{3+}\text{AlSiO}_6$), since these leave no room for additional trivalent substitution. The tetravalent partitioning curves constructed from data of Arzamastsev et al. (2009), Ambrosio and Azzone (2018), and Baudouin et al. (2020) are comparable to ours, despite our high $\text{Ca}_2\text{Al}_2\text{SiO}_6$ component which would be expected to increase the D_{HFSE} (Mollo et al., 2016; Ma and Shaw, 2021).

5.1.5. Olivine $[(M1, M2)_2\text{TO}_4]$

The structure of olivine is composed of a single tetrahedral site occupied by Si^{4+} , and two independent sixfold coordinated octahedral sites M1 and M2, of which the latter is slightly larger (Della et al., 1990; Zanetti et al., 2004). Larger cations (Ca^{2+} , Mn^{2+}) tend to preferentially occupy the M2 site, whereas smaller cations such as transition metals (Ni^{2+} , Co^{2+} , Zn^{2+}) are more commonly observed

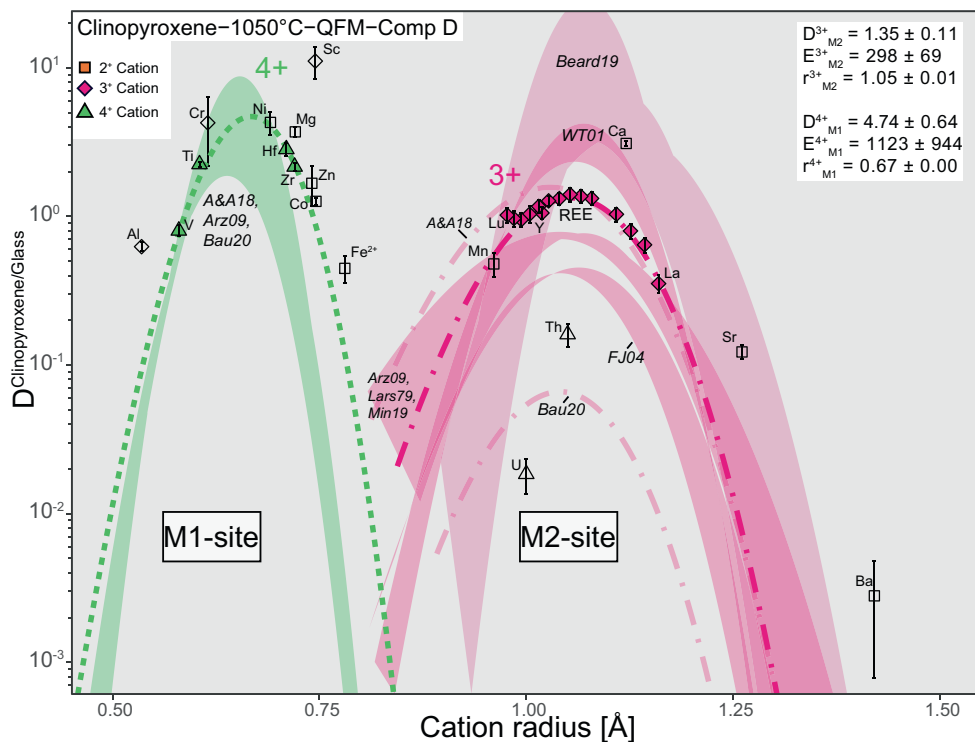


Fig. 10. Representative best-fit lattice strain curves for di- to tetravalent ions in the clinopyroxene structure for a single set of conditions (listed top left). Ionic radii are for six- (M1-site) and eight- (M2-sites) fold coordination taken from Shannon (1976). Abbreviations for sources of literature curves are as follows: A&A18: (Ambrosio and Azzone, 2018), Arz09: (Arzamstev et al., 2009), Bau20: (Baudouin et al., 2020), Beard19: (Beard et al., 2019), FJ04: (Foley and Jenner, 2004), Lars79: (Larsen, 1979), Min19: (Minissale et al., 2019).

to prefer the M1 site. Nevertheless, the similarity in site radius between M1 and M2 allows for interpretation as if these were a single M-site (Zanetti et al., 2004). Divalent partitioning curves suffer from a lack of constraints at low ionic radii and strong dependence on major elements (Fig. 11), on account of which lattice strain parabolas were not built for this valence. Trivalent cations were typically below detection limits in our olivine crystals, but when measured display a parabolic pattern peaking at radii smaller than Sc^{3+} (0.59–0.61 Å; $r_{\text{Sc}}^{\text{VI}} = 0.745$ Å). On account of Al being distributed among tetrahedral and octahedral sites, the trivalent curve is ill-constrained at low radii, leading to a low fitted elastic modulus ($E_{0(M)}^{3+} = 167 - 172$ GPa). However, the expected peak of said curve is in general agreement with the work of Sun and Liang (2013). Tetravalent curves in Onuma diagrams peak at a higher radius (0.59–0.64 Å), with a significantly higher fitted elastic modulus ($E_{0(M)}^{4+} = 922 - 2136$ GPa). Identical treatment of data from chemically similar systems (Larsen, 1979; Foley and Jenner, 2004; Minissale et al., 2019) yields comparable patterns. Trivalent partitioning data on olivine from alkaline systems remain scarce, in part due to the low uptake of REE in the olivine crystal. Those studies which report sufficient partitioning values to construct complete strain parameters (Larsen, 1979; Foley and Jenner, 2004) peak near our lower bound estimates ($r_{0(M)}^{3+} = 0.58 - 0.59$ Å), also with a comparable $D_{0(M)}^{3+}$ (0.19–0.42) in general agreement with olivine from tholeiitic systems (Zanetti et al., 2004; Evans et al., 2008; Sun and Liang, 2013; Dygert et al., 2020). A complete set of tetravalent cation data was only found in the work of Minissale et al. (2019), which indicates an ideal radius of 0.64 Å, and a significantly higher value for $D_{0(M)}^{4+}$ (0.30 vs our 0.01–0.05).

5.1.6. Rhönite [(X)₂(Y)₆(Z)₆O₂₀]

The structure of rhönite is identical to that of aenigmatite, hosting nine M-sites and five T-sites, and is approximated as $(X)_2(Y)_6(Z)_6O_{20}$, in which X, Y, and Z represent the eightfold, sixfold, and fourfold coordinated sites, respectively (Kunzmann, 1989, 1999; Bonaccorsi et al., 1990). Substitution is considered to primarily occur in the X- and Y-sites, and for the Z-site to primarily include Si^{4+} and Ti^{4+} . Monovalent cation incorporation in rhönite is negligible, as reflected by our measurements. Divalent cations are distributed over two sites based on size, with alkaline earth metals and Mn^{2+} partitioning into the larger X-site ($r_{0(X)}^{2+} = 1.03 - 1.08$ Å), and transition metals partitioning into the smaller Y-site ($r_{0(X)}^{2+} = 0.69 - 0.70$). Trivalent cations primarily substitute into the X-site, with the exception of Cr^{3+} , Sc^{3+} , and the heaviest lanthanides (Tm^{3+} , Yb^{3+} , Lu^{3+}) which are observed to transition into the Y-site (Fig. 12). The resulting Y-site curves indicate a site radius close to that of Sc^{3+} (0.67–0.72 Å; $r_{\text{Sc}}^{\text{VI}} = 0.745$ Å), and a high fitted elastic modulus ($E_{0(Y)}^{3+} = 559 - 797$ GPa). The trivalent X-site fit has a radius of approximately 1.04 Å, combined with a significantly lower elastic response of 226–309 GPa. As with divalent cations, the Y-site trivalent curve peaks at a significantly higher value ($D_{0(Y)}^{3+} = 8.56 - 12.72$) than the X-site ($D_{0(X)}^{3+} = 0.16 - 0.22$). Tetrahedral partition coefficient curves adequately agree with the divalent varieties, with an ideal radius of 0.63–0.64 Å for the Y-site, a relatively high value of $D_{0(Y)}^{4+}$ (3.58–5.38) and a high fitted elastic modulus ($E_{0(Y)}^{4+} = 926 - 1523$ GPa). The X-site likely hosts Th^{4+} and U^{4+} , but a strain parabola could not be robustly constructed. Rhönite partitioning has been discussed briefly for experiments by Lofgren et al. (2006), and more thoroughly for natural samples

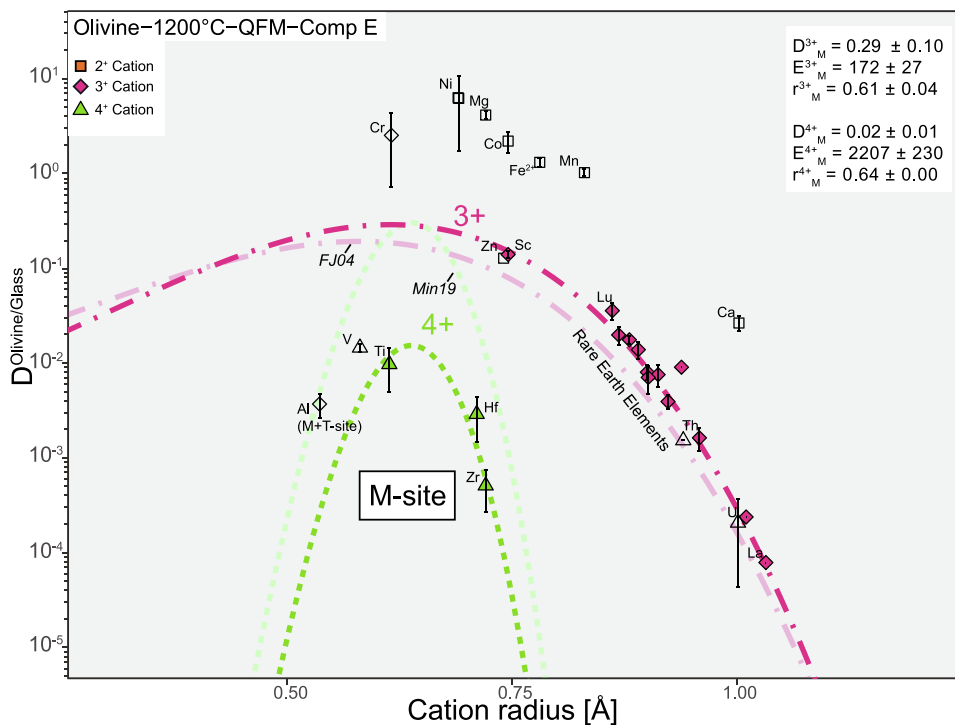


Fig. 11. Representative best-fit Onuma curves for di- to tetravalent ions in the olivine structure for a single set of conditions (listed top left). Ionic radii are for sixfold coordination taken from Shannon (1976). Abbreviations for sources of literature curves are as follows: FJ04: (Foley and Jenner, 2004), Min19: (Minissale et al., 2019).

by Kogarko et al. (2005). The most notable difference between these studies is found with regards to lanthanides, for which Lofgren et al. (2006) reports significantly more incompatible behaviour ($D_{0(X)}^{3+} = 0.05$) compared to the $D_{0(X)}^{3+}$ of 0.58 for the samples of Kogarko et al. (2005) (Fig. 12). An additional distinction is that whereas the samples of Lofgren et al. (2006) display HREE partitioning into the Y-site similar to our experimental products, all HREE in the natural samples of Kogarko et al. (2005) are incorporated into the X-site. This feature is explained through a lack of Fe^{3+} in the compositions of the latter study, causing the electrostatic penalty of introducing REE to be higher, similar to what is observed for clinopyroxene (Beard et al., 2019; Baudouin et al., 2020). Divalent partitioning into the X-site is determined by few elements (Sr^{2+} and Ba^{2+}), which results in both studies being within error of each other. Nevertheless, the data of Kogarko et al. (2005) is also elevated for this valence, and thus our data corresponds better with that of Lofgren et al. (2006). Tetravalent cation incorporation is also elevated in these studies, with D_{Ti} stretching between 6.25 (Kogarko et al., 2005) and 10.68 (Lofgren et al., 2006), in contrast to our reported range of 3.42–5.22. Insufficient data exists to properly discuss trends for this phase.

5.2. Recommended partition coefficients

For use in highly silica-undersaturated, feldspathoid bearing systems we recommend a selection of partition coefficients listed in Table 3. These partition coefficients are the mean values reported for each phase at their approximate liquidus temperature in silica-undersaturated ($\sim\text{SiO}_2 < 42$ wt%), alkali-rich ($\sim\text{Na}_2\text{O} + \text{K}_2\text{O} > 6$ wt%) systems. Though they may well be applicable to more primitive systems as well as to silica-saturated systems, these coefficients should perform best for compositions and conditions similar to those studied here. We believe that for the case of silica-undersaturated, alkali-rich, terrestrial volcanic systems, our values take precedent over those previously reported

on account of (a) being derived under controlled conditions instead of from natural samples, (b) our run products having a clear compositional overlap with those of natural lavas, and (c) our use of natural starting compositions which are both silica-undersaturated and alkali-rich, instead of one or the other. We also supply a more complete range of D-values for a number of phases (3+ in leucite, nepheline), which had so far been left unreported. Caution is advised when applying partition coefficients for elements of particularly low abundance in our starting compositions (e.g., transition metals in low-Mg compositions) to systems more enriched in such elements. Such elements are more subject to detection limits and rounding errors, and may behave differently at higher abundance. Similarly, partition coefficients in hydrous systems may vary substantially from those observed in anhydrous experiments. For more detailed trace element modelling covering a range of temperatures, we supply our complete dataset in Supplementary Material 1.

5.3. Geological application to Nyiragongo

The experimentally derived partition coefficients were used to model the behaviour of trace elements during fractionation processes at Nyiragongo volcano. Specifically, using our newly established partition coefficients, we determined the degree of fractional crystallization necessary to reach the composition of the most recent eruptions (Minissale et al., 2022) of Nyiragongo. Nyiragongo's eruption products are dominated by olivine, clinopyroxene, melilite, nepheline, leucite, oxides, and apatite. Partition coefficients have been measured for the first five of these minerals. For oxides and apatite, partition coefficients are available from Minissale et al. (2019), allowing modelling of all major phases in the system. In order to adequately model the Nyiragongo volcanic system we require a primitive, parental melt composition. Previously Platz et al. (2004) used an olivine melilite composition retrieved from the Rutoke parasitic cone from Denaeyer (1972).

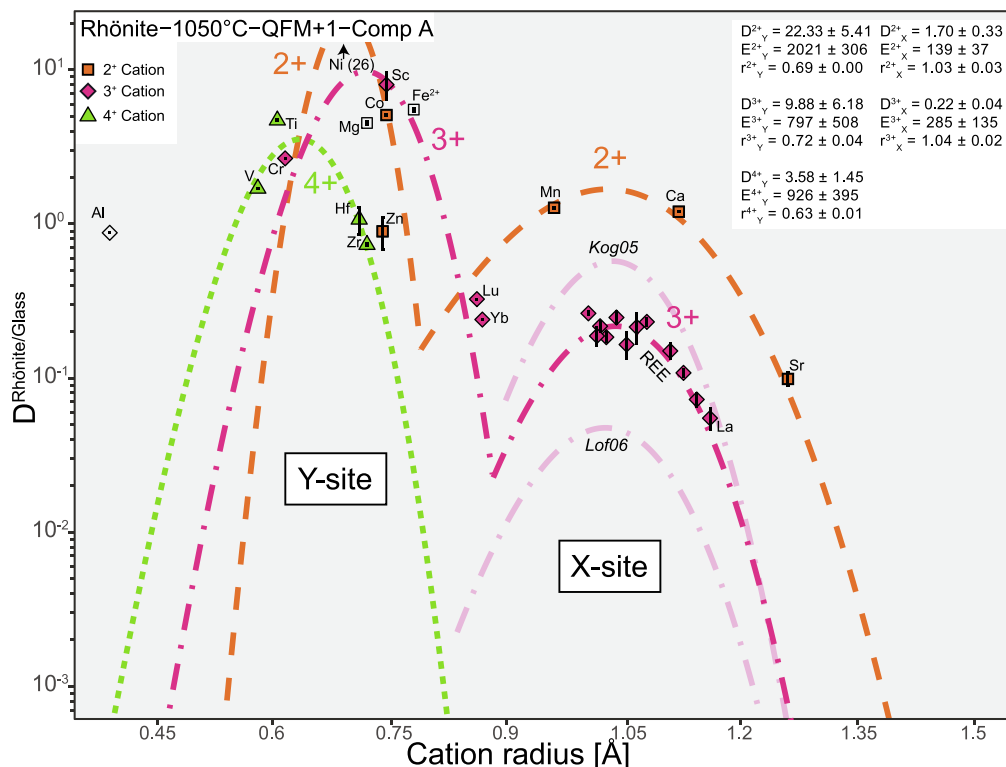


Fig. 12. Representative best-fit Onuma curves for di- to tetravalent ions in the rhönite structure for a single set of conditions (listed top left). Ionic radii are for eight- (X-site), six- (Y-site), and four- (Z-site) fold coordination taken from Shannon (1976). Abbreviations for sources of literature curves are as follows: Kog05: (Kogarko et al., 2005), Lof06: (Lofgren et al., 2006).

However, no trace element data is available for this sample, and we have therefore selected the compositionally similar sample LV1 of Minissale et al. (2022) (MgO = 10.35 wt%) was thus selected. This sample has Rb and Ba concentrations which appear anomalously low for their MgO compared to the rest of the dataset (41, 21, and 116 ppm Rb and 836, 789, and 1862 ppm Ba corresponding to 17.51, **10.35**, and 5.65 wt% MgO samples; LV1 shown in bold). These elements were therefore linearly adjusted to lie directly between their neighbours in terms of MgO (86 ppm Rb, 1457 ppm Ba). A two-step fractionation model was applied, to account for the contrasting mineral assemblages between samples of the parasitic cones and those of the main crater complex (e.g., Demant et al., 1994; Platz et al., 2004; Minissale et al., 2022). The partition coefficients listed in Section 5.3 were used, selecting values for ‘primitive’ compositions (Table 3) for the first fractionation step where possible (only olivine), and the ‘evolved’ values for the second step. Divalent cation partition coefficients for clinopyroxene and all D -values for oxides and apatite were derived from the work of (Minissale et al., 2019).

Trace elements were modelled using the step-wise Rayleigh fractionation equation:

$$C_l = C_0 * F^{(D-1)}$$

wherein C_l is the concentration in the liquid after fractionation, C_0 is the concentration in the parental liquid, F is the fraction of melt over crystallizing material, and D is the bulk partition coefficient of the considered element. The total crystallized fraction was recalculated after each step. Major elements were concurrently modelled using the following equation:

$$C_l = (C_0 - 0.01 * C_f) / F$$

wherein C_l , C_0 , and C_f are the bulk concentrations of a given oxide in the fractionated liquid, starting liquid, and fractionating crystal

assemblage, respectively. For the initial fractionation step we used an adjusted fractionating assemblage based on the one used by Platz et al. (2004) consisting of 60% olivine, 15% melilite, and 25% clinopyroxene, consistent with the mineralogical diversity of the Rushayo chain (Demant et al., 1994). Calculating fractionation for this assemblage to the point of 21% crystallization results in a composition comparable to evolved pyroxene nephelinites described by (Platz et al., 2004), which marks the point at which the fractionating assemblage is changed in the model (Fig. 13). In order to constrain the second fractionation assemblage, we performed a using a least-squares fit Monte-Carlo simulation with varying mineral modes (only including locally minerals found in the natural lavas and using both major and trace element concentrations). This meant that the fractionation model was run for 10,000 arbitrarily determined mineral modes, after each of which the mismatch of the resulting composition with the (average of the) Minissale et al. (2019) glass compositions (in % of both major and trace elements) was calculated. Only the assemblage with the smallest mismatch was kept and is reported below. The 2016 glasses were chosen over the newly reported 2021 lavas (Minissale et al., 2022) in order to filter out potential influence of crystal accumulation on compositional data. Indeed, significant differences in trace element compositions reported by various authors for identical eruptive events were found (Figs. 13, 14), likely due to a combination of analytical uncertainties and variable inclusion of phenocrysts in analysed powders. Therefore, the glasses of Minissale et al. (2019) which were analysed by point- instead of bulk-analysis were deemed most trustworthy.

The best results were obtained using an assemblage of 20% clinopyroxene, 27% melilite, 19% nepheline, <1% leucite, 2% olivine, 25% oxides, and 7% apatite, most likely representing a combination of pyroxene-nephelinite and melilitite lithologies (Demant et al., 1994). By continuing fractionation using this assemblage, the

Table 3

Recommended partition coefficients for main minerals in primitive and evolved systems as indicated by low and high whole-rock MgO. One standard deviation values are listed in brackets following the recommended coefficient. Zero values for standard deviations indicate that only a single measurement was used to constrain the recommended value and standard deviation. See Supplementary Material 1 for a more detailed overview.

Temperature (°C)	Evolved systems (MgO < 10 wt%)						Primitive compositions (MgO > 10 wt%)
	1075	1075	1050	1075	1075	1050	1200
Mineral	Leucite	Melilite	Rhönite	Clinopyroxene	Olivine	Nepheline	Olivine
Cs	17.39 (1.83)	– (–)	0.0255 (0)	0.020 (0.003)	– (–)	0.281 (0.295)	0.921 (0)
Rb	9.23 (0.70)	0.00264 (0.00083)	0.0116 (0.0090)	0.00698 (0.00538)	– (–)	0.676 (0.167)	– (–)
Ba	1.21 (0.17)	0.0356 (0.0035)	0.00583 (0.00479)	– (–)	– (–)	0.0641 (0.0131)	0.000626 (0)
Sr	0.0264 (0.0048)	1.73 (0.25)	0.137 (0.028)	0.000608 (0.000363)	0.369 (0.099)	0.000168 (0.000096)	0.000168 (0.000096)
Co	0.0152 (0.0181)	1.19 (0.15)	4.23 (0.79)	5.43 (0.29)	0.0403 (0.0067)	2.23 (0.50)	2.23 (0.50)
Zn	1.17 (0.57)	0.83 (0.34)	1.08 (0.19)	2.80 (0.62)	0.849 (0.142)	0.13 (0.12)	0.13 (0.12)
Ni	0.112 (0.116)	1.22 (0.37)	18.01 (8.22)	31.47 (2.96)	– (–)	6.29 (3.92)	6.29 (3.92)
La	0.000942 (0.00103)	0.227 (0.029)	0.0475 (0.0071)	0.349 (0.037)	– (–)	0.00119 (0.000491)	0.0000797 (0)
Ce	0.0011 (0.0004)	0.269 (0.031)	0.0732 (0.0104)	0.558 (0.087)	0.0000275.00 (0)	0.00136 (0.00079)	0.000241 (0)
Pr	0.000722 (0.00052)	0.285 (0.032)	0.0948 (0.0130)	0.758 (0.081)	0.00152 (0)	0.00128 (0.00083)	– (–)
Nd	0.00183 (0.00107)	0.289 (0.032)	0.133 (0.019)	0.989 (0.101)	0.00146 (0)	0.00124 (0.00078)	– (–)
Sm	0.00561 (0.00273)	0.251 (0.029)	0.182 (0.036)	1.29 (0.12)	0.00208 (0)	0.00331 (0.00186)	0.00165 (0.00036)
Eu	0.0136 (0.0045)	0.281 (0.030)	0.179 (0.036)	1.30 (0.14)	0.00316 (0)	0.0192 (0.0035)	– (–)
Gd	0.0106 (0.0038)	0.212 (0.028)	0.182 (0.024)	1.43 (0.15)	0.0113 (0)	0.00378 (0.00021)	0.00916 (0)
Tb	– (–)	0.162 (0.020)	0.18 (0.04)	1.36 (0.13)	0.00416 (0)	– (–)	0.00397 (0.00045)
Dy	0.00492 (0)	0.124 (0.019)	0.167 (0.034)	1.28 (0.12)	0.00672 (0)	0.00448 (0.00216)	0.00765 (0.00174)
Y	0.00242 (0.00139)	0.0933 (0.0187)	0.157 (0.037)	1.10 (0.1)	0.0209 (0.0113)	0.00215 (0.00078)	0.00811 (0.00127)
Ho	0.00946 (0.00201)	0.106 (0.020)	0.17 (0.04)	1.18 (0.11)	0.0101 (0.0027)	0.00583 (0.00184)	0.00714 (0.002)
Er	0.00678 (0.00280)	0.075 (0.016)	0.176 (0.052)	1.10 (0.1)	0.0197 (0.0001)	0.00376 (0.00094)	0.014 (0.002)
Tm	– (–)	0.0606 (0.0180)	0.175 (0.072)	1.0 (0.1)	0.0256 (0)	0.00667 (0)	0.0178 (0.0014)
Yb	0.0129 (0)	0.0479 (0.0141)	0.203 (0.047)	0.991 (0.098)	0.0264 (0.0076)	0.00646 (0.00059)	0.0201 (0.0039)
Lu	0.0383 (0.0113)	0.0498 (0.0144)	0.245 (0.069)	1.09 (0.12)	0.0414 (0.0034)	– (–)	0.0361 (0.0058)
Sc	0.181 (0.010)	0.0260 (0.0074)	6.06 (1.71)	17.48 (7.67)	0.304 (0.049)	0.202 (0.034)	0.141 (0.010)
Cr	1.07 (0.57)	0.952 (0.26)	6.24 (3.36)	2.57 (1.26)	3.01 (1.9)	1.14 (0.38)	2.56 (1.58)
Th	0.00236 (0.00123)	0.00468 (0.00142)	0.0114 (0.0040)	0.136 (0.031)	0.000118 (0)	0.000436 (0.000408)	0.00155 (0)
U	0.00476 (0.00271)	0.00186 (0.00105)	0.012 (0.010)	0.0224 (0.0093)	0.000524 (0)	0.000748 (0.000882)	0.00021 (0.00014)
Zr	0.00197 (0.00095)	0.000542 (0.000514)	0.68 (0.06)	2.26 (0.25)	0.002 (0.00072)	0.000721 (0.000620)	0.000518 (0.000211)
Hf	0.0181 (0.0086)	0.0111 (0)	1.11 (0.13)	3.88 (0.70)	0.00769 (0.00309)	0.00316 (0.00074)	0.00294 (0.00119)
V	0.0132 (0.0040)	0.024 (0.007)	1.57 (0.24)	1.12 (0.09)	0.0119 (0.0022)	0.00381 (0.00134)	0.0147 (0.0011)
Nb	0.00266 (0.00241)	0.000766 (0.000802)	0.20 (0.02)	0.11 (0.02)	0.000369 (0.000434)	0.0014 (0.0020)	0.000186 (0.000043)
Ta	0.00705 (0.00407)	0.00131 (0.00039)	0.588 (0.083)	0.463 (0.083)	0.000494 (0.000161)	0.00115 (0.00054)	0.001 (0.001)

2016 glass composition was reached when approximately 48% of the starting melt had crystallized (Figs. 13, 14). The resulting composition adequately matches the 2016 glass compositions in both

major and trace element composition, and has a slightly higher concentration of feldspathoid-incompatible trace elements (e.g. MREE³⁺) than the 2021 eruptive material (Fig. 13c,d, 14b).

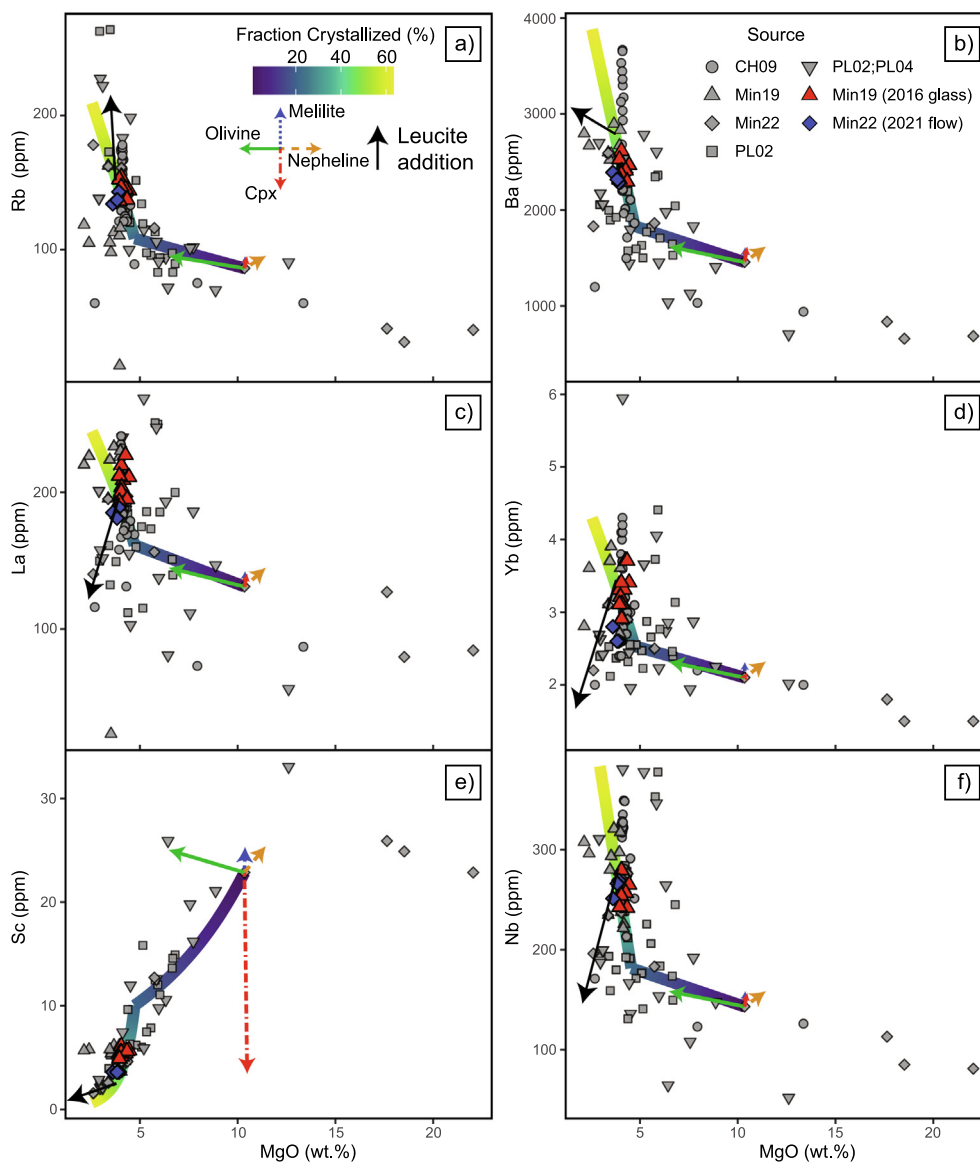


Fig. 13. Binary trace elements (ppm) vs MgO (wt.%) diagrams comparing modelled concentrations with those reported by recent literature. Abbreviations for sources are as follows: CH09: (Chakrabarti et al., 2009), Min19: (Minissale et al., 2019), Min22 (Minissale et al., 2022), PL02: (Platz, 2002), PL04: (Platz et al., 2004). Eruptive material of the 2016 (red triangles) and 2021 (blue diamonds) eruptions have been highlighted. 10% fractionation arrows are included for olivine, melilite, nepheline, and clinopyroxene (cpx) starting from the source composition. An additional arrow of leucite addition is listed, with its origin at the 48% fractionation point. (For interpretation of the references to colour in this figure legend, the reader is referred to the web version of this article.)

Comparison with the 2002 eruptive material suffers from disagreement between authors, with data from Chakrabarti et al. (2009) reporting significantly higher trace element contents for a select group of elements (e.g. Ba^{2+} , Yb^{3+} , Nb^{3+} ; Fig. 13b, d, f). Nevertheless, the remaining dataset and those of other authors (Platz, 2002; Minissale et al., 2019), match our calculated composition within a few percent fractionation. Remaining significant compositional disagreements are for divalent cations, especially transition metals. This is attributed to a combination of low (near zero) concentrations as well as to the lack of well-established partition coefficients for these elements in a variety of phases (also in part due to low concentrations, as well as zoning features).

Leucite is notably missing from our modelled fractionation assemblage despite being a major constituent of the main cone lithologies (e.g., Sahama, 1978; Platz et al., 2004). As a result, the most LILE-rich compositions in the reported datasets cannot be

adequately explained through simple fractionation (Fig. 13a). Instead we argue that, in line with the interpretations of Platz et al. (2004), the majority of leucite crystallization appears limited to the lava-lake system, which leads to accumulation features through floatation (Sahama, 1978), and explains the remaining leucite-rich samples. Simple addition of leucite to our modelled 48% fractionated composition confirms this (Fig. 13).

Rhönite has not been reported for the Nyiragongo volcanic system and has not been included in the modelling. However, rhönite may be important in more shallow fractionating alkali systems such as Cape Verde and the Kaiserstuhl volcanic complex (e.g., Cameron et al. 1970; Kyle and Price 1975; Grapes and Keller 2010; Mata et al. 2017) where it mimics Na-rich clinopyroxene partitioning behaviour in terms of REE^{3+} (Beard et al., 2019; Baudouin et al., 2020), and forms a major sink of HFSE^{4+} .

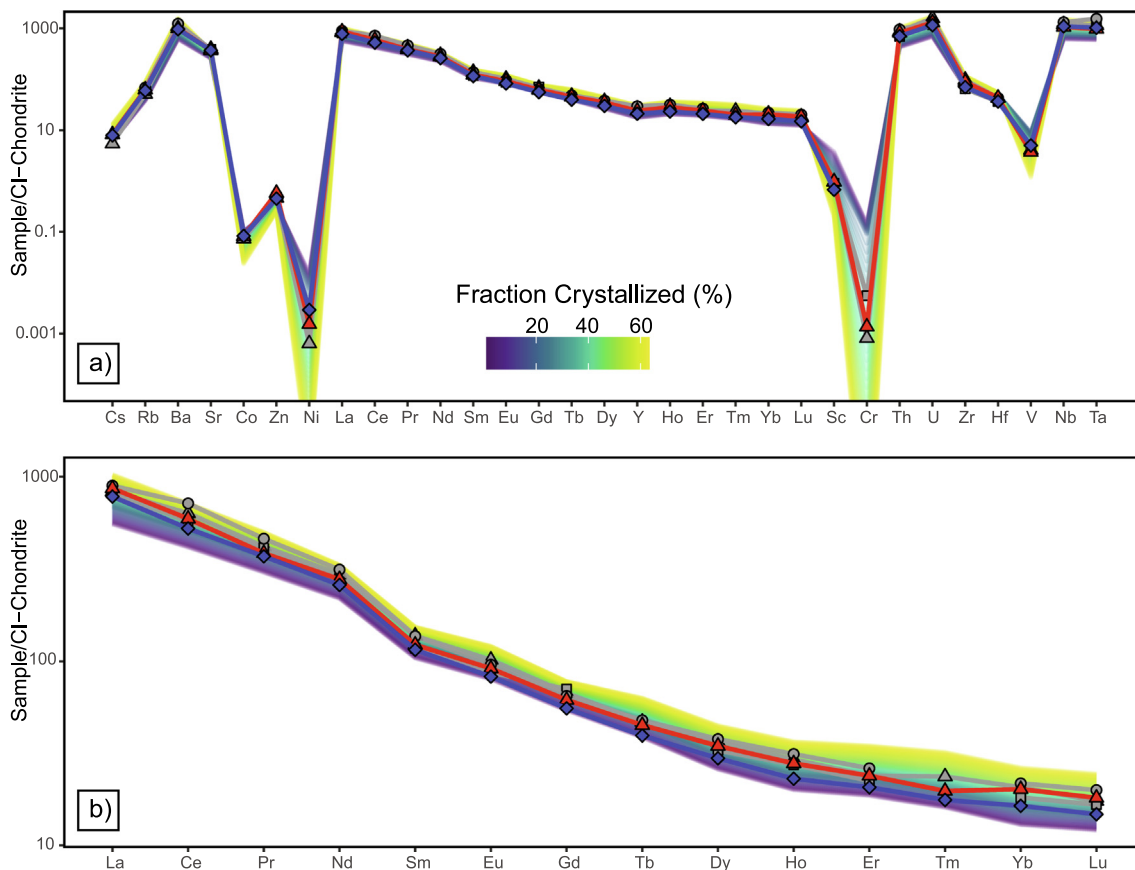


Fig. 14. CI-chondrite normalized (a) trace element- and (b) rare-earth element patterns of the 2002, 2016, and 2021 eruptive materials compared to those resulting from trace element fractionation modelling. Icons for different sources are as listed in Fig. 13. Only data of the 2002 (Platz, 2002; Chakrabarti et al., 2009; Minissale et al., 2019), 2016 (Minissale et al., 2019), and 2021 (Minissale et al., 2022) eruptions is included here. Normalization values are from (McDonough and Sun, 1995).

6. Conclusions

We performed 1 atmosphere gas mixing furnace experiments using alkali-rich, silica-undersaturated whole-rock compositions from the Nyiragongo volcano to determine partition coefficients for phases common in alkali-rich magmatic systems. Experiments were carried out between 1025 °C and 1200 °C with oxygen fugacity buffered to QFM and QFM + 1 in order to investigate the partitioning of trace elements in alkaline magmatic systems.

- Partition coefficients for trace elements of mono- to pentavalent charges were determined for leucite, melilite, nepheline, clinopyroxene, olivine, and rhönite at geologically relevant temperatures. In particular, we present partition coefficients for trivalent to pentavalent cations in the leucite and nepheline structures.
- The lattice strain model (Wood and Blundy, 1997) was used to calculate Onuma diagram parameters in order to allow for extrapolation of trace element partition coefficients.
- A set of trace element partition coefficients applicable for alkali-rich silica-undersaturated settings is proposed (Table 3).
- Fractional crystallization modelling of the Nyiragongo volcanic products using the reported partition coefficients explains progressive enrichment of light over heavy rare earth elements. Our results indicate that 48% crystallization from an olivine melilite basalt composition parental melt reproduces the composition of recent eruptions.
- Our experiments provide insight into phase equilibria for feldspathoid dominated magmatic systems at various fractionation stages under anhydrous, low-pressure conditions.

Declaration of Competing Interest

The authors declare that they have no known competing financial interests or personal relationships that could have appeared to influence the work reported in this paper.

Acknowledgements

The authors would like to thank Benoît Caron and Helen de Waard for their help with LA-ICP-MS analyses. We are additionally grateful to Tilly Bouten and Eric Hellebrand of the Microprobe facility in Utrecht for their assistance. We would like to express our gratitude towards Nicolas Delmelle and Jacqueline Vander Auwera for their assistance with XRF analysis. David A. Neave acknowledges support from NERC (NE/T011106/1). Olivier Namur and Sander M. Molendijk acknowledge support from the FWO through an Odysseus grant to Olivier Namur. Bernard Charlier is a Research Associate of the Belgian Fund for Scientific Research – FNRS. We thank three anonymous reviewers and the handling editor who helped greatly improve this work. We thank the Goma Volcano Observatory (OVG) and the Congolese Institute for Nature Conservation (ICCN) for the provided assistance and necessary authorizations during fieldwork.

Appendix A. Supplementary material

Supplementary material associated with this manuscript can be found in the online version. This includes an overview of all per-

formed experimental runs, including those rejected for analysis, an overview of all major and trace element data, and an summary of calculated Onuma diagram parameters for both our own data and those of previous literature. In addition, we supply an extended discussion on whole-rock geochemical methods, melt compositional evolution and the trace element compositions of crystallized phases. Supplementary material to this article can be found online at <https://doi.org/10.1016/j.gca.2023.01.025>.

References

- Aigner-Torres, M., Blundy, J., Ulmer, P., Pettke, T., 2007. Laser Ablation ICPMS study of trace element partitioning between plagioclase and basaltic melts: An experimental approach. *Contrib. Mineral. Petrol.* 153, 647–667.
- Albarede, F., Bottinga, Y., 1972. Kinetic disequilibrium in trace element partitioning between phenocrysts and host lava. *Geochim. Cosmochim. Acta* 36, 141–156.
- Ambrosio, M.R., Azzone, R.G., 2018. The influence of crystal and melt compositions on the ree+Y partitioning between clinopyroxene and basaltic/tephritic melts of cretaceous alkaline magmatism on the southeastern part of the South American Platform, Southeast Brazil. *Can. Mineral.* 56, 303–329.
- Antao, S.M., Nicholls, J.W., 2018. Crystal chemistry of three volcanic k-rich nepheline samples from oldoinyo lengai, Tanzania and mount nyiragongo, Eastern Congo, Africa. *Front. Earth Sci.* 6.
- Arzamastsev, A.A., Arzamastseva, L.V., Bea, F., Montero, P., 2009. Trace elements in minerals as indicators of the evolution of alkaline ultrabasic dike series: LA-ICP-MS data for the magmatic provinces of northeastern Fennoscandia and Germany. *Petrology* 17, 46–72.
- Barette, F., Poppe, S., Smets, B., Benbakkar, M., Kervyn, M., 2017. Spatial variation of volcanic rock geochemistry in the Virunga Volcanic Province: Statistical analysis of an integrated database. *J. African Earth Sci.* 134, 888–903.
- Barrière, J., Nicolas, D., Smets, B., Oth, A., Delhaye, L., Subira, J., Mashagiro, N., Derauw, D., Smittarello, D., Syavulisebo, A.M., Kervyn, F., 2022. Intra-Crater Eruption Dynamics at Nyiragongo (D.R. Congo), 2002–2021. *J. Geophys. Res. Solid Earth* 127, 2002–2021.
- Baudouin, C., France, L., Boulanger, M., Dalou, C., Luc, J., 2020. Trace element partitioning between clinopyroxene and alkaline magmas: parametrization and role of M1 site on HREE enrichment in clinopyroxenes. *Contrib. Mineral. Petrol.* 175.
- Beard, C.D., van Hinsberg, V.J., Stix, J., Wilke, M., 2019. Clinopyroxene/melt trace element partitioning in sodic alkaline magmas. *J. Petrol.* 44, 92.
- Beattie, P., 1993. Olivine-melt and orthopyroxene-melt equilibria. *Contrib. Mineral. Petrol.* 115, 103–111.
- Beattie, P., Ford, C., Russell, D., 1991. Partition coefficients for olivine-melt and orthopyroxene-melt systems. *Contrib. Mineral. Petrol.* 109, 212–224.
- Beckett, J.R., Spivack, A.J., Hutcheon, I.D., Wasserburg, G.J., Stolper, E.M., 1990. Crystal chemical effects on the partitioning of trace elements between mineral and melt: An experimental study of melilite with applications to refractory inclusions from carbonaceous chondrites. *Geochim. Cosmochim. Acta* 54, 1755–1774.
- Bédard, J.H., 2005. Partitioning coefficients between olivine and silicate melts. *Lithos* 83, 394–419.
- Bédard, J.H., 2006. Trace element partitioning in plagioclase feldspar. *Geochim. Cosmochim. Acta* 70, 3717–3742.
- Bédard, J.H., 2014. Parametrizations of calcic clinopyroxene - Melt trace element partition coefficients. *Geochem. Geophys. Geosyst.* 15, 303–336.
- Bindi, L., Bonazzi, P., Dušek, M., Petříček, V., Chapuis, G., 2001. Five-dimensional structure refinement of natural melilite, (Ca_{1.89}Sr_{0.01}Na_{0.08}K_{0.02})(Mg_{0.92}Al_{0.08})(Si_{1.98}Al_{0.2})O₇. *Acta Crystallogr. Sect. B Struct. Sci.* 57, 739–746.
- Blundy, J.D., Wood, B.J., 1994. Prediction of crystal-melt partition coefficients from elastic moduli. *Nature* 372, 452–454.
- Blundy, J., Wood, B., 2003. Partitioning of trace elements between crystals and melts. *Earth Planet. Sci. Lett.* 210, 383–397.
- Bonaccorsi, E., Merlini, S., Pasero, M., 1990. Rhönite: structural and microstructural features, crystal chemistry and polysomatic relationships. *Eur. J. Mineral.* 2, 203–218.
- Bonechi, B., Perinelli, C., Gaeta, M., Fabbri, A., Petrelli, M., Strnad, L., 2021. High pressure trace element partitioning between clinopyroxene and alkali basaltic melts. *Geochim. Cosmochim. Acta* 305, 282–305.
- Caldwell, D.A., Kyle, P.R., 1994. Mineralogy and Geochemistry of Ejecta erupted from Mount Erebus, Antarctica, Between 1972 and 1986. In: *Volcanological and Environmental Studies of Mount Erebus, Antarctica*, pp. 147–162.
- Cameron, K.L., Carman, M.F., Butler, J.C., 1970. Rhönite from Big Bend National Park, Texas. *Am. Mineral.* 55, 864–874.
- Chakrabarti, R., Basu, A.R., Santo, A.P., Tedesco, D., Vaselli, O., 2009. Isotopic and geochemical evidence for a heterogeneous mantle plume origin of the Virunga volcanics, Western rift, East African Rift system. *Chem. Geol.* 259, 273–289.
- Dalou, C., Boulon, J., Koga, K.T., Dalou, R., Dennen, R.L., 2018. DOUBLE FIT: Optimization procedure applied to lattice strain model. *Comput. Geosci.* 117, 49–56.
- Dawson, J.B., Hinton, R.W., Steele, I.M., 2008. The composition of anorthoclase and nepheline in Mount Kenya phonolite and Kilimanjaro trachyte, and crystal-glass partitioning of elements. *Can. Mineral.* 46, 1455–1464.
- Deer, W.A., Howie, R.A., Zussman, J., 1966. *An Introduction to the Rock Forming Minerals*. Wiley, New York.
- Della, G.A., Ottonello, G., Secco, L., 1990. Precision estimates of interatomic distances using site occupancies, ionization potentials and polarizability in Pbnm silicate olivines. *Acta Crystallogr. Sect. B* 46, 160–165.
- Demant, A., Lestrade, P., Lubala, R.T., Kampunzu, A.B., Durieux, J., 1994. Volcanological and petrological evolution of Nyiragongo volcano, Virunga volcanic field, Zaire. *Bull. Volcanol.* 56, 47–61.
- Denaeyer, M.E., 1972. Les laves du fossé tectonique de l'Afrique Centrale (Kivu, Rwanda, Toro-Ankole): I. Supplément au recueil d'analyses de 1965 II. *Magmatologie III. Magmatogenèse. Musée R. l'Afrique Cent. - Tervuren Belgique Ann. - Série -8°. Sci. Géologiques* 72, 1–134.
- Dollase, W.A., Thomas, W.M., 1978. The crystal chemistry of silica-rich, alkali-deficient nepheline. *Contrib. Mineral. Petrol.* 66, 311–318.
- Dubacq, B., Plunder, A., 2018. Controls on trace element distribution in oxides and silicates. *J. Petrol.* 59, 233–256.
- Durieux, J., 2002. Volcano Nyiragongo (D.R.Congo): Evolution of the crater and lava lakes from the discovery to the present. *Acta Vulcanol.* 14–15, 137–144.
- Dygert, N., Liang, Y., Sun, C., Hess, P., 2014. An experimental study of trace element partitioning between augite and Fe-rich basalts. *Geochim. Cosmochim. Acta* 132, 170–186.
- Dygert, N., Draper, D.S., Rapp, J.F., Lapen, T.J., Fagan, A.L., Neal, C.R., 2020. Experimental determinations of trace element partitioning between plagioclase, pigeonite, olivine, and lunar basaltic melts and an fO₂ dependent model for plagioclase-melt Eu partitioning. *Geochim. Cosmochim. Acta* 279, 258–280.
- Eisele, S., Reißig, S., Freundt, A., Kutterolf, S., Nürnberg, D., Wang, K.L., Kwasnitschka, T., 2015. Pleistocene to Holocene offshore tephrostratigraphy of highly explosive eruptions from the southwestern Cape Verde Archipelago. *Mar. Geol.* 369, 233–250.
- Evans, T.M., Hugh, H.S., Tuff, J., 2008. The influence of melt composition on the partitioning of REEs, Y, Sc, Zr and Al between forsterite and melt in the system CMAS. *Geochim. Cosmochim. Acta* 72, 5708–5721.
- Ewart, A., Griffin, W.L., 1994. Application of proton-microprobe data to trace-element partitioning in volcanic rocks. *Chem. Geol.* 117, 251–284.
- Fabbri, A., Schmidt, M.W., Günther, D., Eikenberg, J., 2008. Experimental determination of radium partitioning between leucite and phonolite melt and 226Ra-disequilibrium crystallization ages of leucite. *Chem. Geol.* 255, 377–387.
- Figowy, S., Dubacq, B., Noël, Y., D'Arco, P., 2020. Partitioning of chromium between garnet and clinopyroxene: First-principle modelling versus metamorphic assemblages. *Eur. J. Mineral.* 32, 387–403.
- Foley, S.F., Jenner, G.A., 2004. Trace element partitioning in lamproitic magmas—the Gaussberg olivine leucite. *Lithos* 75, 19–38.
- Francalanci, L., Peccerillo, A., Poli, G., 1987. Partition coefficients for minerals in potassium-alkaline rocks: Data from Roman province (Central Italy). *Geochem. J.* 21, 1–10.
- Fujimaki, H., 1986. Partition coefficients of Hf, Zr, and REE between zircon, apatite, and liquid. *Contrib. Mineral. Petrol.* 94, 42–45.
- Furman, T., Nelson, W.R., Elkins-Tanton, L.T., 2015. Evolution of the East African rift: Drip magmatism, lithospheric thinning and mafic volcanism. *Geochim. Cosmochim. Acta*, 185.
- Gee, L.L., Sack, R.O., 1988. Experimental petrology of melilite nephelinites. *J. Petrol.* 29, 1233–1255.
- Giordano, D., Polacci, M., Longo, A., Papale, P., Dingwell, D.B., Boschi, E., Kasereka, M., 2007. Thermo-rheological magma control on the impact of highly fluid lava flows at Mt. Nyiragongo. *Geophys. Res. Lett.* 34, 2–5.
- Grapes, R., Keller, J., 2010. Fe²⁺-dominant rhonite in undersaturated alkaline basaltic rocks, Kaiserstuhl volcanic complex, Upper Rhine Graben, SW Germany. *Eur. J. Mineral.* 22, 285–292.
- Green, T.H., Blundy, J.D., Adam, J., Yaxley, G.M., 2000. SIMS determination of trace element partition coefficients between garnet, clinopyroxene and hydrous basaltic liquids at 2–7.5 GPa and 1080–1200°C. *Lithos* 53, 165–187.
- Grove, T.L., 1981. Use of FePt alloys to eliminate the iron loss problem in 1 atmosphere gas mixing experiments: Theoretical and practical considerations. *Contrib. Mineral. Petrol.* 78, 298–304.
- Gualda, G.A.R., Ghiorso, M.S., Lemons, R.V., Carley, T.L., 2012. Rhyolite-MELTS: A modified calibration of MELTS optimized for silica-rich, fluid-bearing magmatic systems. *J. Petrol.* 53, 875–890.
- Hart, S.R., Dunn, T., 1993. Experimental cpx/melt partitioning of 24 trace elements. *Contrib. Mineral. Petrol.* 113, 1–8.
- Hertogen, J., Vanlerberghe, L., Namegabe, M.R., 1985. Geochemical evolution of the Nyiragongo volcano (Virunga, Western African Rift, Zaire). *Bull. Geol. Soc. Finl.* 57, 21–35.
- Hildner, E., Klügel, A., Hansteen, T.H., 2012. Barometry of lavas from the 1951 eruption of Fogo, Cape Verde Islands: Implications for historic and prehistoric magma plumbing systems. *J. Volcanol. Geotherm. Res.* 217–218, 73–90.
- Hill, E., Wood, B.J., Blundy, J.D., 2000. The effect of Ca-Tschermaks component on trace element partitioning between clinopyroxene and silicate melt. *Lithos* 53, 203–215.
- Hill, E., Blundy, J.D., Wood, B.J., 2011. Clinopyroxene-melt trace element partitioning and the development of a predictive model for HFSE and Sc. *Contrib. Mineral. Petrol.* 161, 423–438.
- Hill, E., Blundy, J.D., Wood, B.J., 2012. Erratum to: Clinopyroxene-melt trace element partitioning and the development of a predictive model for HFSE and Sc. *Contrib. Mineral. Petrol.* 163, 563–565.

- Irving, A.J., 1978. A review of experimental studies of crystal/liquid trace element partitioning. *Geochim. Cosmochim. Acta* 42, 743–770.
- Iverson, N.A., Kyle, P.R., Dunbar, N.W., McIntosh, W.C., Pearce, N.J.G., 2014. Eruptive history and magmatic stability of Erebus volcano, Antarctica: Insights from englacial tephra. *Geochem. Geophys. Geosyst.* 15, 4180–4202.
- Jensen, B.B., 1973. Patterns of trace element partitioning. *Geochim. Cosmochim. Acta* 37, 2227–2242.
- Jia, Y.Q., 1991. Radii and Effective Ionic Radii of the Rare Earth Ions. *J. Solid State Chem.* 95, 184–187.
- Johnson, K.T.M., 1998. Experimental determination of partition coefficients for rare earth and high-field-strength elements between clinopyroxene, garnet, and basaltic melt at high pressures. *Contrib. Mineral. Petrol.* 133, 60–68.
- Jung, C., Jung, S., Hoffer, E., Berndt, J., 2006. Petrogenesis of Tertiary Mafic Alkaline Magmas in the Hoheifel, Germany. *J. Petrol.* 47, 1637–1671.
- Karato, S.I., 2016. Physical basis of trace element partitioning: A review. *Am. Mineral.* 101, 2577–2593.
- Keppeler, H., 1996. Constraints from partitioning experiments on the composition of subduction-zone fluids. *Nature* 380, 237–240.
- Klaudius, J., Keller, J., 2006. Peralkaline silicate lavas at Oldoinyo Lengai, Tanzania. *Lithos* 91, 173–190.
- Kogarko, L.N., Hellebrand, E., Ryabchikov, I.D., 2005. Trace element partitioning between rhönite and silicate melt in Cape Verde volcanics. *Geochem. Int.* 43, 3–9.
- Komorowski, J.-C., Tedesco, D., Kasereka, M., Allard, P., Papale, P., Vaselli, O., Durieux, J., Baxter, P., Halbwegs, M., Akumbe, M., Baluku, B., Briole, P., Ciraba, M., Dupin, J.-C., Etoy, O., Garcin, D., Hamaguchi, H., Houlié, N., Kavotha, K.S., Lemarchand, A., Lockwood, J., Lukaya, N., Mavonga, G., de Michele, M., Mporo, S., Mukambilwa, K., Munyololo, F., Newhall, C., Ruch, J., Yalire, M., Wafula, M., 2002. The January 2002 flank eruption of Nyiragongo volcano (Democratic Republic of Congo): chronology, evidence for a tectonic rift trigger, and impact of lava flows on the city of Goma. *Acta Vulcanol.* 14, 27–62.
- Kuehner, S.M., Laughlin, J.R., Grossman, L., Johnson, M.L., Burnett, D.S., 1989. Determination of trace element mineral/liquid partition coefficients in melilite and diopside by ion and electron microprobe techniques. *Geochim. Cosmochim. Acta* 53, 3115–3130.
- Kunzmann, T., 1989. Rhönit: Mineralchemie, Paragenese und Stabilität in alkalibasaltischen Vulkaniten, Ein Beitrag zur Mineralogenese der Rhönit-änigmatit-Mischkristallgruppe. Universität München.
- Kunzmann, T., 1999. The aenigmatite-rhönite mineral group. *Eur. J. Mineral.* 11, 743–756.
- Kyle, P.R., Moore, J.A., Thirlwall, M.F., 1992. Petrologic evolution of anorthoclase phonolite lavas at Mount Erebus, Ross island, Antarctica. *J. Petrol.* 33, 849–875.
- Kyle, P., Price, R., 1975. Occurrences of Rhönite in Alkalic Lavas of the McMurdo Volcanic Group, Antarctica, and Dunedin Volcano, New Zealand. *Am. Mineral.* 60, 722–725.
- Larsen, L.M., 1979. Distribution of REE and other trace elements between phenocrysts and peralkaline undersaturated magmas, exemplified by rocks from the Gardar igneous province, south Greenland. *Lithos* 12, 303–315.
- Lee, C.T.A., Harbert, A., Leeman, W.P., 2007. Extension of lattice strain theory to mineral/mineral rare-earth element partitioning: An approach for assessing disequilibrium and developing internally consistent partition coefficients between olivine, orthopyroxene, clinopyroxene and basaltic melt. *Geochim. Cosmochim. Acta* 71, 481–496.
- Lindsley, D.H., 1983. Pyroxene thermometry. *Am. Mineral.* 68, 477–493.
- Lofgren, G.E., Huss, G.R., Wasserburg, G.J., 2006. An experimental study of trace-element partitioning between Ti-Al-clinopyroxene and melt: Equilibrium and kinetic effects including sector zoning. *Am. Mineral.* 91, 1596–1606.
- Lundstrom, C.C., Shaw, H.F., Ryerson, F.J., Williams, Q., Gill, J., 1998. Crystal chemical control of clinopyroxene-melt partitioning in the Di-Ab-An system: Implications for elemental fractionations in the depleted mantle. *Geochim. Cosmochim. Acta* 62, 2849–2862.
- Lundstrom, C.C., Sutton, A.L., Chaussidon, M., McDonough, W.F., Ash, R., 2006. Trace element partitioning between type B CAI melts and melilite and spinel: Implications for trace element distribution during CAI formation. *Geochim. Cosmochim. Acta* 70, 3421–3435.
- Lustrino, M., Wilson, M., 2007. The circum-Mediterranean anorogenic Cenozoic igneous province. *Earth-Sci. Rev.* 81, 1–65.
- Ma, S., Shaw, C.S.J., 2021. An experimental study of trace element partitioning between peridotite minerals and alkaline basaltic melts at 1250°C and 1 GPa: crystal and melt composition impacts on partition coefficients. *J. Petrol.* 62.
- Martin, A.P., Cooper, A.F., Price, R.C., 2013. Petrogenesis of Cenozoic, alkalic volcanic lineages at Mount Morning, West Antarctica and their entrained lithospheric mantle xenoliths: Lithospheric versus asthenospheric mantle sources. *Geochim. Cosmochim. Acta* 122, 127–152.
- Mata, J., Martins, S., Mattielli, N., Madeira, J., Faria, B., Ramalho, R.S., Silva, P., Moreira, M., Caldeira, R., Moreira, M., Rodrigues, J., Martins, L., 2017. The 2014–15 eruption and the short-term geochemical evolution of the Fogo volcano (Cape Verde): Evidence for small-scale mantle heterogeneity. *Lithos* 288–289, 91–107.
- Matzen, A.K., Baker, M.B., Beckett, J.R., Wood, B.J., Stolper, E.M., 2017. The effect of liquid composition on the partitioning of Ni between olivine and silicate melt. *Contrib. to Mineral. Petrol.* 172, 1–18.
- McDonough, W.F., Sun, S.S., 1995. The composition of the Earth. *Chem. Geol.* 120, 223–253.
- Minissale, S., Zanetti, A., Tedesco, D., Morra, V., Melluso, L., 2019. The petrology and geochemistry of Nyiragongo lavas of 2002, 2016, 1977 and 2017 AD, and the trace element partitioning between melilitite glass and melilite, nepheline, leucite, clinopyroxene, apatite, olivine and Fe-Ti oxides: a unique scenario. *Lithos* 332–333, 296–311.
- Minissale, S., Casalini, M., Cucciniello, C., Balagizi, C., Tedesco, D., Boudoire, G., Morra, V., Melluso, L., 2022. The geochemistry of recent Nyamulagira and Nyiragongo potassic lavas, Virunga Volcanic Province, and implications on the enrichment processes in the mantle lithosphere of the Tanzania-Congo craton. *Lithos* 420–421, 106696.
- Mittlefehldt, D.W., Miller, C.F., 1983. Geochemistry of the Sweetwater Wash Pluton, California: Implications for “anomalous” trace element behavior during differentiation of felsic magmas. *Geochim. Cosmochim. Acta* 47, 109–124.
- Mollo, S., Forni, F., Bachmann, O., Blundy, J.D., De Astis, G., Scarlato, P., 2016. Trace element partitioning between clinopyroxene and trachy-phonolitic melts: A case study from the Campanian Ignimbrite (Campi Flegrei, Italy). *Lithos* 252–253, 160–172.
- Morrison, A., Whittington, A., Smets, B., Kervyn, M., Sehlke, A., 2020. The rheology of crystallizing basaltic lavas from Nyiragongo and Nyamuragira volcanoes, D.R.C. *Volcanica* 3, 1–28.
- Mungall, J.E., Martin, R.F., 1995. Petrogenesis of basalt-comendite and basalt-pantellerite suites, Terceira, Azores, and some implications for the origin of ocean-island rhyolites. *Contrib. Mineral. Petrol.* 119, 43–55.
- Nagasawa, H., Schreiber, H.D., Morris, R.V., 1980. Experimental Mineral/Liquid Partition Coefficients of the Rare Earth Elements (REE) Sc and Sr for Perovskite, Spinel and Melilite. *Earth Planet. Sci. Lett.* 46, 431–437.
- Namur, O., Humphreys, M.C.S., 2018. Trace element constraints on the differentiation and crystal mush solidification in the Skaergaard intrusion, Greenland. *J. Petrol.* 59, 387–418.
- Neumann, E.-R., Wulff-Pedersen, E., Simonsen, S.L., Pearson, N.J., Marti, J., Mitjavila, J., 1999. Evidence for Fractional Crystallization of Periodically Refilled Magma Chambers in Tenerife, Canary Islands. *J. Petrol.* 40, 1089–1123.
- Onuma, N., Higuchi, H., Wakita, H., Nagasawa, H., 1968. Trace element partition between two pyroxenes and the host lava. *Earth Planet. Sci. Lett.* 5, 47–51.
- Onuma, N., Onuma, N., Ninomiya, S., Nagasawa, H., Nagasawa, H., 1981. Mineral/groundmass partition coefficients for nepheline, melilite, clinopyroxene and perovskite in melilite-nepheline basalt, Nyiragongo. *Zaire. Geochim. J.* 15, 221–228.
- Platz, T., 2002. Nyiragongo Volcano, DR Congo: Mineral Chemistry and Petrology. University of Greifswald, Germany. PhD Thesis.
- Platz, T., Foley, S.F., André, L., 2004. Low-pressure fractionation of the Nyiragongo volcanic rocks, Virunga Province, D.R. Congo. *J. Volcanol. Geotherm. Res.* 136, 269–295.
- Poppe, S., Smets, B., Fontijn, K., Rukeza, M.B., De Marie Fikiri Migabo, A., Milungu, A. K., Namogo, D.B., Kervyn, F., Kervyn, M., 2016. Holocene phreatomagmatic eruptions alongside the densely populated northern shoreline of Lake Kivu, East African Rift: timing and hazard implications. *Bull. Volcanol.* 78.
- Pottier, Y., 1978. Première éruption historique du Nyiragongo et manifestations adventives simultanées du volcan Nyamuragira (chaîne des Virungues-Kivu-Zaire: Déc 76 - Juin 77). *Mus R Afr Centr-Tervuren Belg, Dépt Géol Min Rapp ann*, pp. 157–175.
- Poulet, A., Bellon, H., Bram, K., 2016. The Cenozoic volcanism in the Kivu rift: Assessment of the tectonic setting, geochemistry, and geochronology of the volcanic activity in the South-Kivu and Virunga regions. *J. African Earth Sci.* 121, 219–246.
- Pupier, E., Duchene, S., Toplis, M.J., 2008. Experimental quantification of plagioclase crystal size distribution during cooling of a basaltic liquid. *Contrib. Mineral. Petrol.* 155, 555–570.
- Putirka, K.D., 2016. Rates and styles of planetary cooling on Earth, Moon, Mars, and Vesta, using new models for oxygen fugacity, ferric-ferrous ratios, olivine-liquid Fe-Mg exchange, and mantle potential temperature. *Am. Mineral.* 101, 819–840.
- Regenauer-Lieb, K., Rosenbaum, G., Lyakhovskiy, V., Liu, J., Weinberg, R., Segev, A., Weinstein, Y., 2015. Melt instabilities in an intraplate lithosphere and implications for volcanism in the Harrat Ash-Shaam volcanic field (NW Arabia). *J. Geophys. Res. Solid Earth* 120, 1543–1558.
- Sahama, T.G., 1962. Petrology of Mt. Nyiragongo: a review. *Trans. Edinburgh Geol. Soc.* 19, 1–28.
- Sahama, T.G., 1978. The Nyiragongo main cone. *Musée R. l’Afrique Cent. - Tervuren Belgique Ann. - Série -8°. Sci. Géologiques* 81, 88.
- Shannon, R.D., 1976. Revised effective ionic radii and systematic studies of interatomic distances in halides and chalcogenides. *Acta Crystallogr. Sect. A* 32, 751–767.
- Shepherd, K., Namur, O., Toplis, M.J., Devidal, J.L., Charlier, B., 2022. Trace element partitioning between clinopyroxene, magnetite, ilmenite and ferrobasaltic to dacitic magmas: an experimental study on the role of oxygen fugacity and melt composition. *Contrib. Mineral. Petrol.* 177, 1–21.
- Skulski, T., Minarik, W., Watson, E.B., 1994. High-pressure experimental trace-element partitioning between clinopyroxene and basaltic melts. *Chem. Geol.* 117, 127–147.
- Smyth, J.R., Bish, D.L., 1988. Crystal Structures and Cation Sites of the Rock-Forming Minerals.

- Spampinato, L., Ganci, G., Hernández, P.A., Calvo, D., Tedesco, D., Pérez, N.M., Calvari, S., Del Negro, C., Yalire, M.M., 2013. Thermal insights into the dynamics of Nyiragongo lava lake from ground and satellite measurements. *J. Geophys. Res. Solid Earth* 118, 5771–5784.
- Sun, C., Graff, M., Liang, Y., 2017. Trace element partitioning between plagioclase and silicate melt: The importance of temperature and plagioclase composition, with implications for terrestrial and lunar magmatism. *Geochim. Cosmochim. Acta* 206, 273–295.
- Sun, S.S., Hanson, G.N., 1976. Rare earth element evidence for differentiation of McMurdo volcanics, Ross Island, Antarctica. *Contrib. to Mineral. Petrol.* 54, 139–155.
- Sun, C., Liang, Y., 2012. Distribution of REE between clinopyroxene and basaltic melt along a mantle adiabat: Effects of major element composition, water, and temperature. *Contrib. Mineral. Petrol.* 163, 807–823.
- Sun, C., Liang, Y., 2013. The importance of crystal chemistry on REE partitioning between mantle minerals (garnet, clinopyroxene, orthopyroxene, and olivine) and basaltic melts. *Chem. Geol.* 358, 23–36.
- Tait, K.T., Sokolova, E., Hawthorne, F.C., Khomyakov, A.P., 2003. The crystal chemistry of Nepheline. *Can. Mineral.* 41, 61–70.
- Taura, H., Yurimoto, H., Kurita, K., Sueno, S., 1998. Pressure dependence on partition coefficients for trace elements between olivine and the coexisting melts. *Phys. Chem. Miner.* 25, 469–484.
- Tazieff, H., 1949. Première exploration du cratère du volcan Nyiragongo. *Bull. la Société Belge Géologie* 58, 165–172.
- Tazieff, H., 1984. Mt. Nyiragongo: renewed activity of the lava lake. *J. Volcanol. Geotherm. Res.* 20, 267–280.
- Tepley, F.J., Lundstrom, C.C., McDonough, W.F., Thompson, A., 2010. Trace element partitioning between high-An plagioclase and basaltic to basaltic andesite melt at 1 atmosphere pressure. *Lithos* 118, 82–94.
- Tilley, E.C., Thompson, R.N., 1972. Melting relations of some ultra alkali volcanics. *Geol. J.* 8, 65–70.
- Tomlinson, E.L., Smith, V.C., Menzies, M.A., 2020. Chemical zoning and open system processes in the Laacher See magmatic system. *Contrib. Mineral. Petrol.* 175, 1–18.
- Ustunisik, G., Ebel, D.S., Walker, D., Nielsen, R.L., Gemma, M., 2019. Trace element partitioning between CAI-type melts and grossite, melilite, hibonite, and olivine. *Geochim. Cosmochim. Acta* 267, 124–146.
- Van Westrenen, W., Allan, N.L., Blundy, J.D., Purton, J.A., Wood, B.J., 2000. Atomistic simulation of trace element incorporation into garnets-comparison with experimental garnet-melt partitioning data. *Geochim. Cosmochim. Acta* 64, 1629–1639.
- Viccaro, M., Calcagno, R., Garozzo, I., Giuffrida, M., Nicotra, E., 2015. Continuous magma recharge at Mt. Etna during the 2011–2013 period controls the style of volcanic activity and compositions of erupted lavas. *Mineral. Petrol.* 109, 67–83.
- Volfinger, M., Robert, J.L., 1980. Structural control of the distribution of trace elements between silicates and hydrothermal solutions. *Geochim. Cosmochim. Acta* 44, 1455–1461.
- Wagner, J., Haigis, V., Künzel, D., Jahn, S., 2017. Trace element partitioning between silicate melts – A molecular dynamics approach. *Geochim. Cosmochim. Acta* 205, 245–255.
- Welsch, B., Hammer, J., Baronnet, A., Jacob, S., Hellebrand, E., Sinton, J., 2016. Clinopyroxene in postshield Haleakala ankaramite: 2. Texture, compositional zoning and supersaturation in the magma. *Contrib. Mineral. Petrol.* 171, 1–19.
- Wiedenmann, D., Zaitsev, A.N., Britvin, S.N., Krivovichev, S.V., Keller, J., 2009. Alumoåkermanite, $(Ca, Na)_2(Al, Mg, Fe^{2+})(Si_2O_7)$, a new mineral from the active carbonatite-nephelinite-phonolite volcano Oldoinyo Lengai, northern Tanzania. *Mineral. Mag.* 73, 373–384.
- Wood, B.J., Blundy, J.D., 1997. A predictive model for rare earth element partitioning between clinopyroxene and anhydrous silicate melt. *Contrib. Mineral. Petrol.* 129, 166–181.
- Wood, B.J., Blundy, J.D., 2014. Trace Element Partitioning: The Influences of Ionic Radius, Cation Charge, Pressure, and Temperature. In: *Treatise on Geochemistry*. Second Edition. Elsevier Ltd., pp. 327–353.
- Wood, B.J., Trigila, R., 2001. Experimental determination of aluminous clinopyroxene-melt partition coefficients for potassic liquids, with application to the evolution of the Roman province potassic magmas. *Chem. Geol.* 172, 213–223.
- Wright, R., Blackett, M., Hill-Butler, C., 2015. Some observations regarding the thermal flux from Earth's erupting volcanoes for the period of 2000 to 2014. *Geophys. Res. Lett.* 42, 282–289.
- Zanetti, A., Tiepolo, M., Oberti, R., Vannucci, R., 2004. Trace-element partitioning in olivine: Modelling of a complete data set from a synthetic hydrous basanite melt. *Lithos* 75, 39–54.